Palaeogeography, Palaeoclimatology, Palaeoecology 654 (2024) 112455

Contents lists available at ScienceDirect

Palaeogeography, Palaeoclimatology, Palaeoecology

journal homepage: www.elsevier.com/locate/palaeo

# Millennial-scale sedimentary evolution of carbonate platforms during the Permian–Triassic boundary hyperthermal event

Jiawei He [a], Xiumian Hu [b], Juan Li [c], David B. Kemp [d], Mingcai Hou [a], Zhong Han [a,*]

[a] State Key Laboratory of Oil and Gas Reservoir Geology and Exploitation, Institute of Sedimentary Geology, Chengdu University of Technology, Chengdu 610059, China
[b] State Key Laboratory of Mineral Deposit Research, School of Earth Sciences and Engineering, Nanjing University, Nanjing 210023, China
[c] State Key Laboratory of Palaeobiology and Stratigraphy, Nanjing Institute of Geology and Palaeontology, Chinese Academy of Sciences, Nanjing 210008, China
[d] State Key Laboratory of Biogeology and Environmental Geology and Hubei Key Laboratory of Critical Zone Evolution, School of Earth Sciences, China University of Geosciences, Wuhan 430074, China

## ARTICLE INFO

Editor: Bing Shen

*Keywords:*
Permian–Triassic boundary
Carbon isotope
Carbonate microfacies
Xenoconformity
Carbonate platform

## ABSTRACT

The millennial-scale response of shallow-water carbonate platforms to the climatic upheaval at the Permian–-Triassic boundary (PTB) remains unclear. This study presents three carbonate platform sections across the Permian–Triassic (P–T) boundary in South China and the Lhasa terrane. A total of 14 types of carbonate microfacies were identified, which show that the Liangfengya and Taiping sections in South China were deposited in an inner ramp, and the Wenbudangsang section on the Lhasa terrane was deposited in an outer ramp. Bulk carbonate carbon isotope patterns through the sections are generally characterized by negative excursions (−2.2 to −3.5‰) during the PTB hyperthermal event. These excursions can be divided into four phases (NC1 to NC4), with NC1 before the negative carbon isotope excursion (NCIE) event, NC2 during the initiation phase of the NCIE, NC3 during the body of the NCIE, and the NC4 marking the recovery stage of the NCIE. The pattern of sedimentary changes in each section through the PTB hyperthermal event, and the relationship between these changes and the carbon isotope stages, was established. In the studied sections, the onset of the NCIEs (NC2 stage) preceded evidence for a carbonate production crisis, with the occurrence of anachronistic facies developed after this crisis but prior to the NC3 stage. In detail, our data show that the carbonate production crisis occurred 11 kyr after the onset of the NCIE, and 47 kyr before the first Permian–Triassic mass extinction (PTME), and that the carbonate production crisis may have been closely related to the environmental stresses associated with greenhouse gas emission from the Siberian Traps Large Igneous Province (STLIP).

## 1. Introduction

The Permian–Triassic boundary (PTB) witnessed the largest mass extinction ever recorded in Earth's history, with 90% of marine and 70% of terrestrial species disappearing (Shen et al., 2011a; Song et al., 2012; Wang et al., 2014; Fan et al., 2020; Mays et al., 2021). The event was characterized by a marked global negative carbon isotope excursion (NCIE) related to large-scale emission of $^{12}$C-enriched carbon. This was contemporaneous with global warming, with an increase in surface seawater temperatures by as much as 8–10 °C (Sun et al., 2012; Song et al., 2021a; Joachimski et al., 2012; Chen et al., 2016; Foster et al., 2018; Hu et al., 2020). These factors led to severe climatic changes and environmental stress, such as ocean acidification (Georgiev et al., 2011; Hinojosa et al., 2012; Jurikova et al., 2020; Song et al., 2021b), redox changes (Shen et al., 2016; Fang et al., 2021; Newby et al., 2021; Chen et al., 2022a), productivity changes (Algeo et al., 2013; Shen et al., 2015; Du et al., 2020), the displacement of vegetation and ecosystem collapse (Yu et al., 2015; Feng et al., 2020; Xu et al., 2022), and enhanced continental weathering (Sun et al., 2018; Cao et al., 2019, though see also Xu et al., 2023). Greenhouse gas emission from the Siberian Traps Large Igneous Province (STLIP) is generally believed to have been the main driving force for the mass extinction and associated environmental changes (Joachimski et al., 2019; Shen et al., 2019a, 2019b). In addition, large-scale acidic volcanic eruptions in South China have recently been postulated as a potential kill mechanism involved in the mass extinction (Zhang et al., 2021).

There have been several methods employed to track environmental changes during the PTB hyperthermal event, including traditional

---

* Corresponding author.
*E-mail address:* hanzhong19@cdut.edu.cn (Z. Han).

https://doi.org/10.1016/j.palaeo.2024.112455
Received 1 December 2023; Received in revised form 17 August 2024; Accepted 17 August 2024

isotopes (e.g., O, S, N) (Luo et al., 2011; Shen et al., 2011b; Schobben et al., 2014; Chen et al., 2016, 2020; Sun et al., 2019; Liao et al., 2020), organic geochemistry (e.g., TOC, biomarkers) (Sawada et al., 2012; Kaiho et al., 2021), and nontraditional isotopes (e.g., Hg, Zn, Ni, U) (Liu et al., 2017; Zhang et al., 2020a; Shen et al., 2022a). However, the impacts of PTB environmental changes on sedimentary systems are relatively poorly known. In particular, the responses of shallow-water carbonate platforms (e.g., production rates, facies changes) are unclear, with our knowledge of platform evolution through the PTB hindered by a lack of correlation between platforms developed at different paleolatitudes (Tian et al., 2014, 2019; Li et al., 2019). Microfacies analysis of PTB-aged platforms has been conducted at sites from South China, Iran, Hungary, Slovenia, and southern Tibet (Dolenec et al., 2004; Haas et al., 2006; Hips and Haas, 2009; Tian et al., 2014, 2019; Li et al., 2019; Maaleki-Moghadam et al., 2019; Gliwa et al., 2020). Generally, these studies have documented that carbonate microfacies during the PTB hyperthermal event underwent a rapid transition from bioclastic packstone, wackestone, to bioclast-free or low bioclast content mudstone, limestone, or dolomite. At the same time, there is a lack of discussion on the evolution and relative timing of some specific events during the PTB hyperthermal, such as the carbonate productivity crisis, occurrence of anachronistic facies (cf. Woods, 2014), and mass extinction events. Moreover, the previous studies noted above are generally from a single section or site. In addition, due to the absence of conodonts in some sections, the PTB hyperthermal event is mainly determined by the paleontological assemblages of other fossils or the NCIE (Dolenec et al., 2004; Haas et al., 2006; Hips and Haas, 2009; Fio et al., 2010; Korte and Kozur, 2010; Shen et al., 2013).

In this study, three biostratigraphically well-constrained PTB sections from South China and the Lhasa terrane have been studied using high-resolution analysis of carbonate microfacies and bulk carbonate carbon isotopes. Using carbonate microfacies analysis, changes in sedimentary environment and biological changes were determined to evaluate changes in carbonate production rates under different

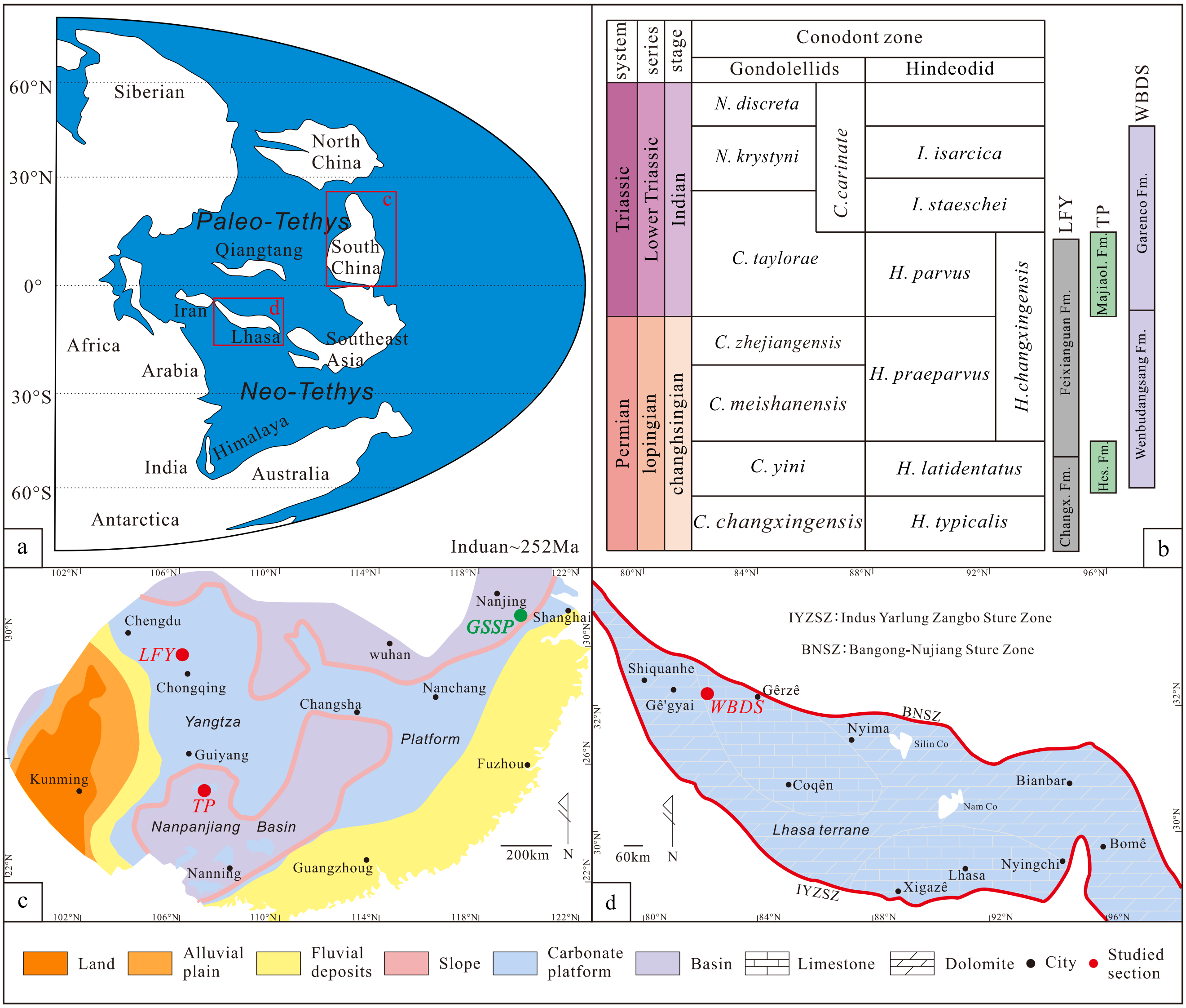

**Fig. 1.** Geologic and paleogeographic maps. (a) Paleogeographic reconstruction in the Late Permian (modified from Ziegler et al., 1997) showing the location of South China and Lhasa. (b) Timescale and conodont zones for the Lopingian to the Lower Triassic (modified from Algeo et al., 2013) showing the conodont zonation in the Liangfengya section (LFY) (Yuan and Shen, 2011; Li et al., 2021a), Taiping section (TP) (Lehrmann et al., 2003; Xiao et al., 2018), and Wenbudangsang section (WBDS) (Wu et al., 2014). (c) Late Permian paleogeographic map of south China showing the locations of the Liangfengya section at Chongqing and Taiping section at Guangxi studied (modified from Lehrmann et al., 2003; Yin et al., 2014). (d) Late Permian paleogeographic map of the Lhasa terrane (modified from Wu et al., 2021) showing the location of the Wenbudangsang section. Changx. Fm.: Changxing Formation; Hes. Fm.: Heshan Formation; Majiaol. Fm.: Majiaoling Formation; *C.*: *Clarkina*; *H.*: *Hindeodus*; *N.*: *Neogondolella*; I.: *Isarciella*; Fm.: Formation; GSSP: global boundary stratotype section and point.

environments. Using carbon isotopes as a chemostratigraphic tool, the coupled evolution between carbonate microfacies and carbon-isotope perturbations was established. Based on this, the evolution of the platforms at the millennial-scale was reconstructed.

## 2. Geologic background

During the latest Permian, South China was located at a low latitude near the equator in the northern hemisphere (Fig. 1a) (Ziegler et al., 1997; Zhou et al., 2016). The interior was mainly covered by marine deposits (Yangtze platform), which are bounded by the Kangdian Oldland to the east and by the Cathaysia Block to the west (Yin et al., 2014). Compared to South China, the Lhasa Terrane in the Late Permian was located at a low latitude in the southern hemisphere and formed an isolated carbonate platform on the southern margin of the Paleo-Tethys Ocean (Wu et al., 2021; Shen et al., 2023) (Fig. 1a).

### *2.1. Liangfengya section, Chongqing (South China)*

The Liangfengya section is located on the Yangtze platform near the city of Chongqing (Fig. 1c) (Yuan and Shen, 2011). It crops out in a disused quarry in the Zhongliangshan anticline (Fig. 2a, b and c). The measured stratigraphic thickness of the section is 41.3 m, comprising the Late Permian Changxing Formation and the Early Triassic Feixianguan Formation. The Changxing Formation is 9.85 m thick and mainly consists of medium- to thick-bedded gray bioclastic limestone with abundant fossils, including foraminifera, calcareous green algae, and echinoderms (Wignall and Twitchett, 1999; Jia and Song, 2018). Black siliceous nodules are also observed. The uppermost Changxing Formation is assigned to the *Clarkina changxingensis* Zone in Late Permian Changxingian (Fig. 1b) (Yuan and Shen, 2011; Li et al., 2021a). The overlying Feixianguan Formation has a thickness of 31.45 m. The lower part is dominated by a thick-bedded argillaceous limestone with few fossils, with echinoderms being the main component and several mudstone layers occur in it. The upper part is dominated by thick-bedded mudstones, with muddy layers of 1–2 cm thickness wide parallel to the bedding, and no fossils are found. The Feixianguan Formation corresponds to the conodont zones of *Clarkina yini*, *Clarkina meishanensis* and *Hindeodus praeparvus* (Fig. 1b) (Yuan and Shen, 2011; Li et al., 2021a). According to the first appearance datum (FAD) of *Hindeodus parvus*, the PTB is located at a height of 11.3 m (Yuan and Shen, 2011; Li et al., 2021a), 1.51 m above the base of the Feixianguan Formation.

### *2.2. Taiping section, Guangxi (South China)*

The Taiping section was located on the Great Bank of Guizhou in South China during the Late Permian and is located at Taiping village, Pingguo town, Guangxi (Fig. 1c) (Lehrmann et al., 2003). The measured stratigraphic thickness of the section is 40.7 m (Fig. 2d and e, f), and

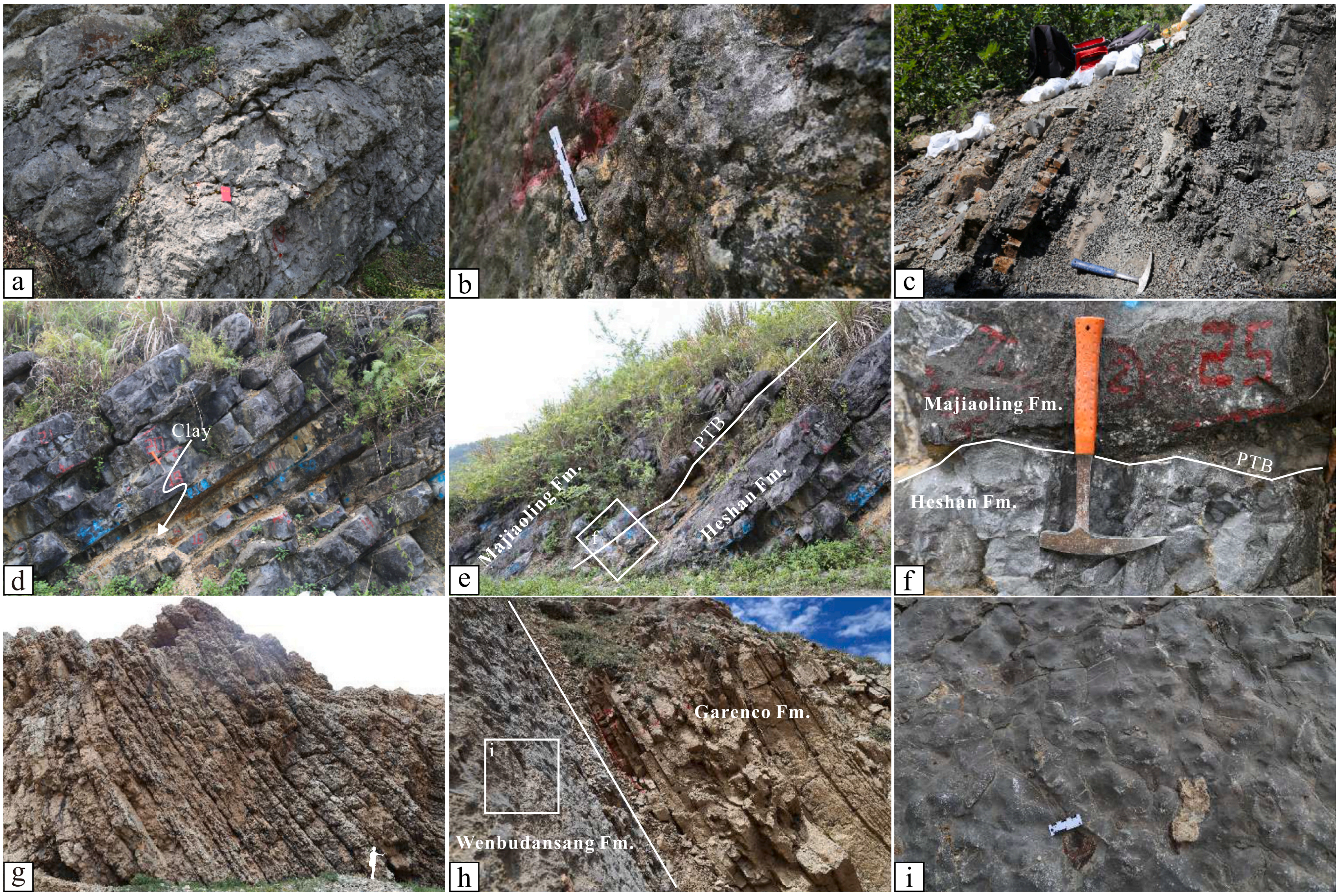

**Fig. 2.** Outcrop photographs of the Liangfengya (a-c), Taiping (d-f), and Wenbudangsang (g-i) sections. (a) Thin- to medium-bedded limestone in the Changxing Formation. (b) Macroscopic image of the xenoconformity. (c) Thin-bedded limestone in the Feixianguan Formation. (d) The Heshan Formation showing an intermediate clay layer and thin- to medium-bedded limestone. (e) The PTB and the boundary of the xenoconformity (white line). (f) The xenoconformity boundary between the Heshan and Majiaoling Formations (white line). (g) Medium-bedded limestone in the Wenbudangsang Formation (person for scale is ~1.8 m high). (h) The xenoconformity boundary between the Wenbudangsang and Garenco Formations (white line). (i) The xenoconformity between the Wenbudangsang and Garenco Formations.

comprises the Late Permian Heshan Formation and the Early Triassic Majiaoling Formation. The Heshan Formation is 9.5 m thick and consists of medium- to thick-bedded gray bioclastic limestone. Abundant fossils are observed, including foraminifera, calcareous green algae, and bivalves. It contains several layers of mudstone (Tian et al., 2019), as well as black siliceous nodules. The Heshan Formation corresponds to the *Hindeodus latidentatus* Zone (Fig. 1b) (Lehrmann et al., 2003; Xiao et al., 2018), which indicates the Changxingian Stage of Late Permian. The overlying Majiaoling Formation is 31.2 m thick. The lower part consists of gray microbialite with few fossils but some occasional ostracods (Bagherpour et al., 2017). The upper part consists mainly of medium to thick gray-blackish limestone. Stylolite structures and ostracods are occasionally observed. In the lower part of the Majiaoling Formation, *Hindeodus parvus* is identified (Xiao et al., 2018), indicating the Induan Stage of the Early Triassic (Fig. 1b). According to the FAD of *Hindeodus parvus*, the PTB is located at the lower part of the Majiaoling Formation (Lehrmann et al., 2003; Xiao et al., 2018), 9.5 m above the base.

### *2.3. Wenbudangsang section, Geji (Lhasa terrane)*

The Wenbudangsang section from the Lhasa terrane (Fig. 1d) is located about 10 km east of Wenbudangsang village near Geji county, central Tibet. This section is 51.5 m thick (Fig. 2g and h, i). It is composed of the Late Permian Wenbudangsang Formation and the Early Triassic Garenco Formation. The measured Wenbudangsang Formation is 12.7 m thick and consists of medium-bedded gray to dark gray limestone with some brachiopods (Ji et al., 2018). Siliceous nodules are also observed. The Wenbudangsang Formation contains the *Clarkina yini*, *Clarkina meishanensis* zones and part of the *Hindeodus praeparvus* zones (Fig. 1b) (Wu et al., 2014), indicating the Late Permian Changxingian Stage. The overlying Garenco Formation is 38.8 m thick. The lower part is mainly composed of dolomite and dolomitic limestone, with few fossils. The upper part is mainly medium-bedded gray limestone. The Garenco Formation corresponds to part of the conodont zone *Hindeodus praeparvus*, indicating the Changxingian Stage of the Late Permian, and the conodont zones of *Hindeodus parvus*, *Isarciella staeschei*, *Isarciella isarcica*, indicating the Early Induan Stage of Early Triassic (Fig. 1b) (Wu et al., 2014). According to the FAD of *Hindeodus parvus*, the PTB is 0.26 m above the base of the Garenco Formation (Wu et al., 2014), at 12.96 m in our measured section.

## 3. Methods

A total of 420 samples were collected from the Liangfengya, Taiping, and Wenbudangsang sections, using sampling resolutions of 0.3–0.5 m, 0.2–0.3 m, and 0.5–1 m, respectively. The sample spacing across the PTB in the sections was reduced to ~0.1 m. During sampling, only fresh samples without later alteration, calcite veins, and obvious weathering were collected to ensure the reliability of the environmental reconstruction and geochemical data. Samples were made into rock thin-sections for microfacies analysis and were also used for inorganic carbon and oxygen isotope analysis.

### *3.1. Carbonate microfacies analysis*

Microfacies classification was based on comprehensive optical microscope analysis of thin sections and hand samples. Grain types, matrix, fossil composition, terrigenous content (mainly quartz), dolomitization, bioturbation, and other sedimentary structures were recorded. Carbonates were classified according to the nomenclature of Dunham (1962) and Embry and Klovan (1971). Carbonate microfacies were compared with the standard microfacies and environmental interpretations of Flügel (2010).

### *3.2. Stable carbon and oxygen isotope analysis*

Bulk carbon and oxygen isotope analysis of samples from the 3 sections were determined at the State Key Laboratory for Mineral Deposits Research, Nanjing University. Samples were powdered using a microdrill. During the drilling process, visible calcite veins and shells were avoided. The powder of each sample was weighed and sent to a prototype automatic Gas Bench II, where the sample was reacted with $H_3PO_4$ at 70 °C to produce $CO_2$, before passing into a Finnigan AMT delta plus XP mass spectrometer. Isotope data are expressed in Vienna Pee Dee Belemnite Standard (VPDB) delta notation (δ). The analytical precision (1σ) was 0.05‰ and 0.07‰ for $\delta^{13}C$ and $\delta^{18}O$, respectively.

### *3.3. Xenoconformity analysis*

A xenoconformity is a stratigraphic interface that occurs due to a fundamental, sudden, and permanent transition in sedimentary facies, extending from the basin scale to the global scale (Carroll, 2017). The cause is taken to be a rapid, significant, and irreversible change in paleoenvironment (Carroll, 2017; Gao et al., 2021), such as an abrupt change in paleo-water depth, paleoclimate, or paleo-marine environment. Xenoconformities are characterized by abrupt changes in lithology, sedimentary facies or facies assemblages, biological extinction, geophysical interface, and geochemistry (Carroll, 2017; Gao et al., 2021). It is well known that sudden, global-scale changes in oceanic environments occurred during the PTB, including ocean acidification, widespread anoxia, productivity changes, and increases in surface seawater temperatures (Hinojosa et al., 2012; Joachimski et al., 2012; Algeo et al., 2013; Shen et al., 2016; Song et al., 2021b; Newby et al., 2021; Chen et al., 2022a, 2022b), which could have resulted in pervasive xenoconformity development. In this study, we used the above-mentioned criteria to identify xenoconformities during the PTB.

## 4. Results

### *4.1. Carbonate microfacies*

Based on field observations, sedimentological features, fossiliferous assemblages, textures, and fabrics, 14 microfacies (MF1 to MF14) can be identified in the Liangfengya, Taiping, and Wenbudangsang sections. Together, these represent a carbonate ramp environment and can be further divided into three sedimentary environments including inner ramp, middle ramp, and outer ramp (Table 1, Figs. 3–5).

#### *4.1.1. Inner ramp*

*4.1.1.1. MF1: microbialite.* The microbialites are dominated by calcified cyanobacteria (10–15%) and ostracods (5%). The facies can be further divided into laminated microbialite and dendritic microbialite (Fig. 3a and b). This microfacies occurs only in the medium to thick-bedded limestone in the lower part of the Majiaoling Formation from the Taiping section (Fig. 5).

Cyanobacteria are mostly photosynthetic organisms that mainly occur in warm and shallow marine environments. Calcified cyanobacteria in the Paleozoic mainly occur in rocks deposited in the intertidal and subtidal zones (Flügel, 2010; Tang et al., 2017; Zhang et al., 2020b). The micritic matrix, the presence of cyanobacteria, and the predominantly laminated structure, together with the large diameter (average around 10 μm) of framboidal pyrite (Xiao et al., 2018), suggests an oxic shallow peritidal environment in an inner ramp.

*4.1.1.2. MF2: calcareous green algae wackestone.* This microfacies is characterized by calcareous green algae in the micritic matrix (Fig. 3c). The calcareous green algae are dominated by Dasycladales and Gymnocodiaceae (30–40%). Other biotic grains (5–15%) include fusulinid,

**Table 1**
Average composition, sedimentary structure, and depositional environment in the Liangfengya, Taiping, and Wenbudangsang sections.

| | Microfacies | Carbonate grains/% | | | | | | | | TC/% | Matrix/% | Sedimentary structure | Depositional environment |
|---|---|---|---|---|---|---|---|---|---|---|---|---|---|
| | | CA | B | F | E | Os | CS | Cy | Ca | | | | |
| MF1 | Microbialite | – | – | – | – | 5–8 | – | 10–12 | – | – | 5 | | shallow peritidal |
| MF2 | Calcareous green algae wackestone | 35–60 | 5–7 | 10–15 | 5 | – | – | – | – | – | 20–30 | | shallow back–reef |
| MF3 | Benthic foraminiferal wackestone | 5 | – | 25–30 | 5 | – | – | – | – | – | 40 | Stylolite | very shallow marine |
| MF4 | Calcareous spicule wackestone | 3 | 3 | 5 | – | – | 20–30 | – | – | – | 20 | | shallow marine |
| MF5 | Bioclastic grainstone | 10–15 | 4 | 40–45 | 5 | 3 | – | – | – | – | 40 | Micritic envelope | adjacent open ramp |
| MF6 | Sandy mudstone | – | – | – | – | – | – | – | – | 15–20 | 40 | | shallow subtidal |
| MF7 | Argillaceous bioclastic wackestone | – | 5 | 5–10 | 15–20 | – | – | – | – | <5 | 30–50 | Micritic envelope | shallow open marine |
| MF8 | Crinoidal wackestone | – | 2 | 5 | 15–20 | – | – | – | – | – | 40–50 | | Shallow marine |
| MF9 | Mudstone | – | – | – | – | – | – | – | – | – | 90–95 | Bioturbation | deep subtidal or upper intertidal |
| MF10 | Dolomitized mudstone | – | 5 | – | – | 3 | – | – | – | – | 80–90 | Lamellar | deep supratidal or upper intertidal |
| MF11 | Fine-crystalline dolostone | – | – | – | – | – | – | – | – | – | – | | middle ramp |
| MF12 | Storm-affected mudstone | – | 5 | – | 10–20 | – | – | – | – | – | 50–60 | Erosive contact | above storm wave base |
| MF13 | Burrowed bioclastic wackestone | – | 10 | – | 3 | – | – | – | – | – | 80–90 | Bioturbation | below storm wave base |
| MF14 | Calcisphere mudstone | – | – | – | – | – | – | – | 3–10 | – | 90–90 | | Outer ramp |

CA: calcareous algae; B: bivalves; F: foraminifer; E: echinoderm; Os: ostracods; CS: calcareous spicule; Cy: cyanobacteria; Ca: calcisphere; TC: terrigenous clast

small benthic foraminifera, fragments of echinoderm, and bivalve. This microfacies is mainly observed in the Changxing Formation from the Liangfengya section and the Heshan Formation from the Taiping section (Figs. 4 and 5).

Dasycladales thrive in the upper part of the photic zone at a depth of 0–10 m, Dasycladales mainly live in open-inner ramps or back-reef environments (Banner and Simmons, 1994; Flügel, 2010). Well-preserved and high-abundance calcareous green algae, together with the micritic matrix, indicate deposition in a very shallow back-reef environment.

*4.1.1.3. MF3: benthic foraminiferal wackestone.* This microfacies is dominated by benthic foraminifera and fusulinids (25–30%) (Fig. 3d). Rare calcareous green algae and echinoderm fragments are also observed. The matrix is mainly micrite and is locally dolomitized, showing stylolite structure. MF3 occurs in the middle to the upper part of the Changxing Formation in the Liangfengya section and the lowermost part of the Heshan Formation in the Taiping section (Figs. 4 and 5).

Fusulinid and benthic foraminifera are generally considered to live in water depths of tens of metre (Flügel, 2010). Calcareous green algae thrive in the upper part of the photic zone. The micritic matrix, together with fusulinid and benthic foraminifera, thus points to a very shallow marine environment.

*4.1.1.4. MF4: calcareous spicule wackestone.* This microfacies has bioclasts that are dominated by calcareous sponge spicules (20–30%) with minor calcareous green algae and bivalve fragments (Fig. 3e). The matrix is mainly micritic. This microfacies occurs only in the lower part of the Heshan Formation in the Taiping section (Fig. 5).

In contrast to siliceous sponge spicules, which are common in basinal environments, calcareous sponge spicules can occur in shallow water (Flügel, 2010; James and Jones, 2015). Additionally, this microfacies appears as interbeds in MF2 and the calcareous green algae occur together with the micritic matrix. A shallow marine environment is thus inferred.

*4.1.1.5. MF5: bioclastic grainstone.* This microfacies is characterized by small benthic foraminifera, fusulinid and calcareous green algae set in a sparry cement (45–50%) (Fig. 3f). Other bioclasts (5–8%) include fragments of echinoderms, bivalves, and ostracods, which locally have a micritic envelope and are mostly well-preserved. MF5 is mainly found in the middle to upper part of the Heshan Formation in the Taiping section (Fig. 5).

This microfacies is mainly characterized by a grain-supported texture with sparry calcite. Considering lack of the micritic matrix and relatively abundant bioclasts, an inner ramp environment with relatively strong water agitation adjacent to an open ramp is likely (Flügel, 2010).

*4.1.1.6. MF6: sandy mudstone.* This microfacies is characterized by silt- to sand-sized quartz (15–20%) set in a micritic matrix (Fig. 3g). Rare pyrite is also observed in the matrix. This microfacies occurs only in the middle of the Heshan Formation in the Taiping section (Fig. 5) and is interbedded with strata containing calcareous green algae (MF2).

The micritic matrix indicates a relatively low-energy environment (Flügel, 2010). A shallow subtidal environment influenced by terrigenous clastic inputs is suggested given its close association with MF2.

*4.1.1.7. MF7: argillaceous bioclastic wackestone.* This microfacies is dominated by fragments of echinoderms (10–20%) with benthic foraminifera (5–10%) as a subordinate component. The matrix is mainly micrite, with argillaceous material locally (Fig. 3h). MF7 occurs only in the uppermost of the Feixianguan Formation and directly overlies MF3 in the Liangfengya section (Fig. 4).

Low-energy background mudstone deposition frequently affected by argillaceous input suggests deposition in low-energy marine environments. Considering its occurrence stratigraphically adjacent to the MF3, a shallow open marine environment is inferred.

*4.1.1.8. MF8: crinoidal wackestone.* This microfacies is dominated by crinoids (20%) in micrite. The crinoids partly display micritic envelopes. Other (rarer) fossils include well-preserved calcareous green algae, benthic foraminifera, and bivalve fragments (Fig. 3i). This microfacies occurs mainly in the Feixianguan Formation of the Liangfengya section at Chongqing (Fig. 4).

Abundant and densely packed crinoid fragments represent a specific facies type formed in various settings including slopes, restricted platforms, reefs, and mounds (Flügel, 2010). Considering the microfacies combination of mudstone (MF9) above and argillaceous bioclastic wackestone (MF7) below, it is inferred to have been deposited in a

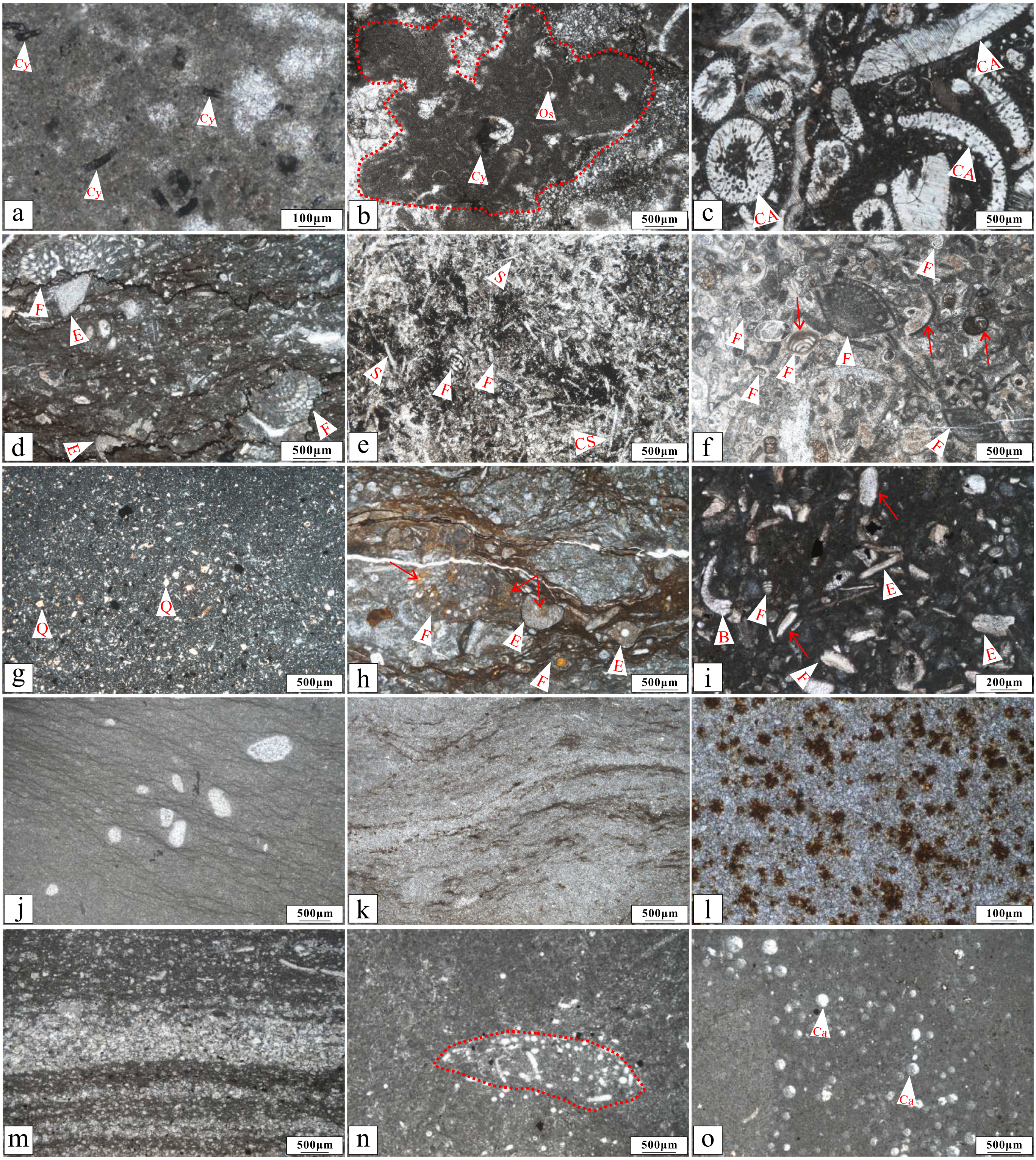

**Fig. 3.** Thin section photos of representative microfacies. (a) MF1 microbialite. (b) Cross-section through microbialite (red dashed line). (c) MF2 calcareous green algae wackestone. (d) MF3 benthic foraminiferal wackestone. (e) MF4 calcareous spicule wackestone. (f) MF5 bioclastic grainstone showing micritic envelope (red arrow). (g) MF6 sandy mudstone. (h) MF7 argillaceous bioclastic wackestone, showing the chambers filled with clayey material (red arrow). (i) MF8 crinoidal wackestone, showing micritic envelope (red arrow). (j) MF9 mudstone. (k) MF10 dolomitized mudstone showing lamellar features. (l) MF11 fine-crystalline dolostone. (m) MF12 storm-affected mudstone, showing the erosive contact with background deposits (red dashed line). (n) MF13 burrowed bioclastic wackestone showing bioturbation structure (red dashed line). (o) MF14 calcisphere mudstone. Cy: cyanobacteria; Os: ostracods; CA: calcareous green algae; B: bivalves; F: foraminifera; E: echinoderms; CS: calcareous spicules; Q: quartz; Ca: calcisphere. (For interpretation of the references to colour in this figure legend, the reader is referred to the web version of this article.)

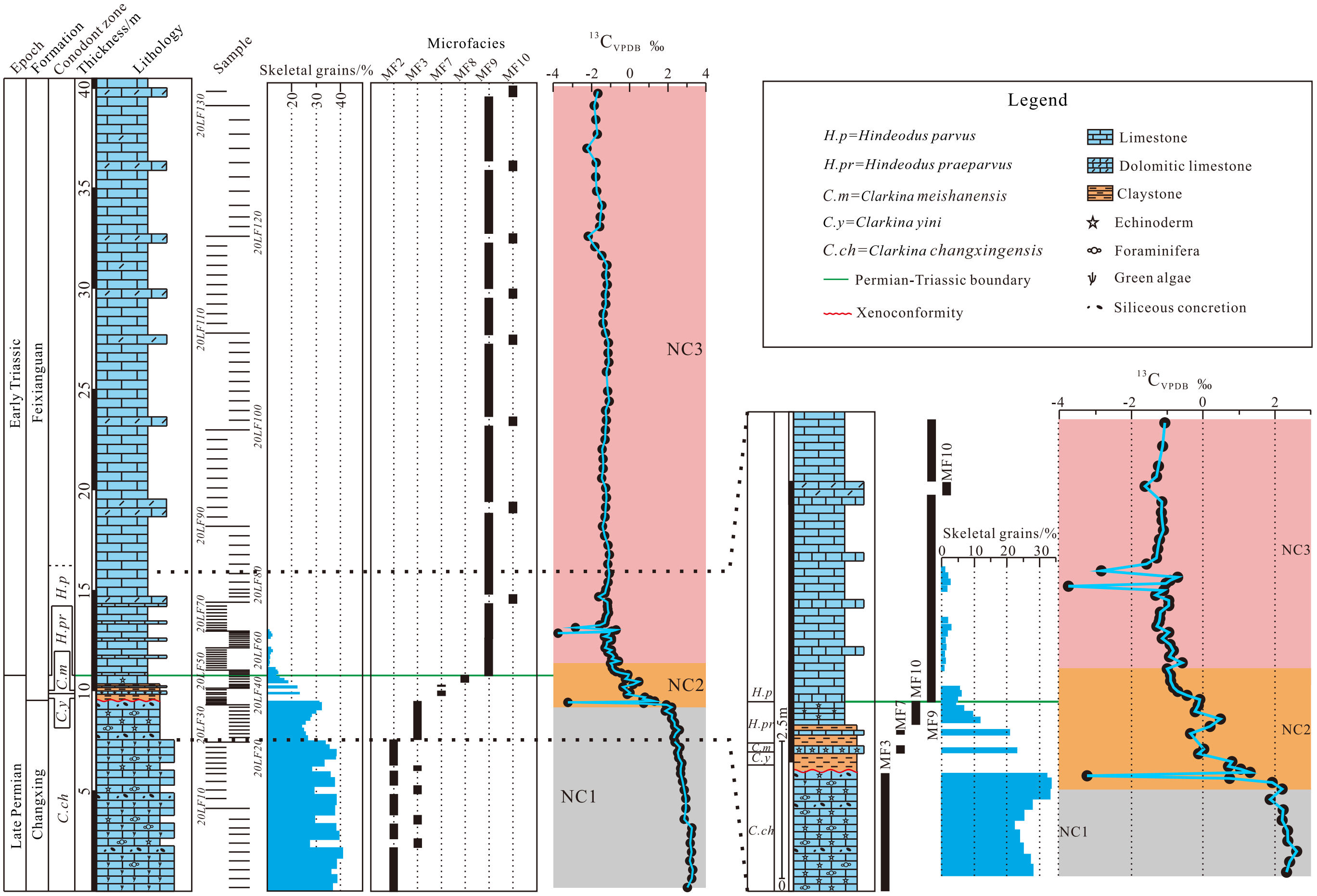

**Fig. 4.** Stratigraphic log of the Liangfengya section showing sampling locations, biostratigraphy, bioclast distribution, microfacies classification, whole-rock carbonate $\delta^{13}C$ curve, enlarged view of the NC2 stage, and conodont zones after Yuan and Shen (2011) and Li et al. (2021a). VPDB: Vienna Pee Dee Belemnite.

shallow marine inner platform environment.

#### 4.1.1.9. MF9: mudstone.

This microfacies is dominated by micrite with a paucity of fossils and bioturbation structures (Fig. 3j). MF9 is widely developed in the Feixianguan Formation in the Liangfengya section and the Majiaoling Formation in the Taiping section (Figs. 4 and 5).

Non-laminated mudstones lacking fossils and structures may suggest a deep subtidal zone or upper intertidal zone with relatively quiet water and abnormal salinity (Flügel, 2010).

#### 4.1.1.10. MF10: dolomitized mudstone.

This microfacies alternates with MF10 and is dominated by micrite with rare bioclasts (4–5%), including ostracods and bivalves (Fig. 3k). The micritic matrix is selectively dolomitized, which locally have lamellar features. MF10 occurs mainly in the Feixianguan Formation in the Liangfengya section at Chongqing and in the Majiaoling Formation in the Taiping section at Guangxi (Figs. 4 and 5).

Low-energy background mudstone deposition with selective dolomitization, and rare fossils and structures, may suggest a depositional environment adjacent to but more open that of MF9, and hence a deep supratidal zone or upper intertidal environment (Flügel, 2010).

### 4.1.2. Middle ramp

#### 4.1.2.1. MF11: fine-crystalline dolostone.

This microfacies is characterized by euhedral to subhedral dolomite crystals (Fig. 3l). No obvious bioclasts or bioturbation is observed. This microfacies is found only in the lowermost part of the Garenco Formation in the Wenbudangsang section (Fig. 6),

There are several mechanisms to interpret the origin of dolostone (e.g., intense evaporation, microbial activity, sulfate-reducing microorganisms) (Li et al., 2018, 2023; Warthmann et al., 2000). As such, the occurrence of dolostone alone cannot be used to indicate any specific depositional environment. In this section, MF11 is interbedded with MF12 and MF13 (see description and interpretation below), suggesting deeper water near the middle ramp depositional environment.

#### 4.1.2.2. MF12: storm-affected mudstone.

This microfacies is dominated by bivalves and fragments of echinoderms (10–20%). The matrix is mainly micrite. Centimetre-scale beds formed of thin-shelled bivalves are observed and these display parallel laminae (Fig. 3m). This microfacies occurs at the lower part of the Garenco Formation in the Wenbudangsang section (Fig. 6).

Background mudstone suggests a low-energy environment. Thin-shelled bivalve beds with parallel laminae suggest deposition during the weakening phase of storms. (Flügel, 2010; Pérez-López and Pérez-Valera, 2011). Low-energy background mudstone deposition frequently interrupted by storm events suggests deposition in a middle ramp section above storm wave base.

### 4.1.3. Outer ramp

#### 4.1.3.1. MF13: burrowed bioclastic wackestone.

This microfacies is characterized by fragments of bivalves, echinoderms, and micro-bioclasts set in a micritic matrix (Fig. 3n). Bioturbation is widely developed in the Wenbudangsang Formation.

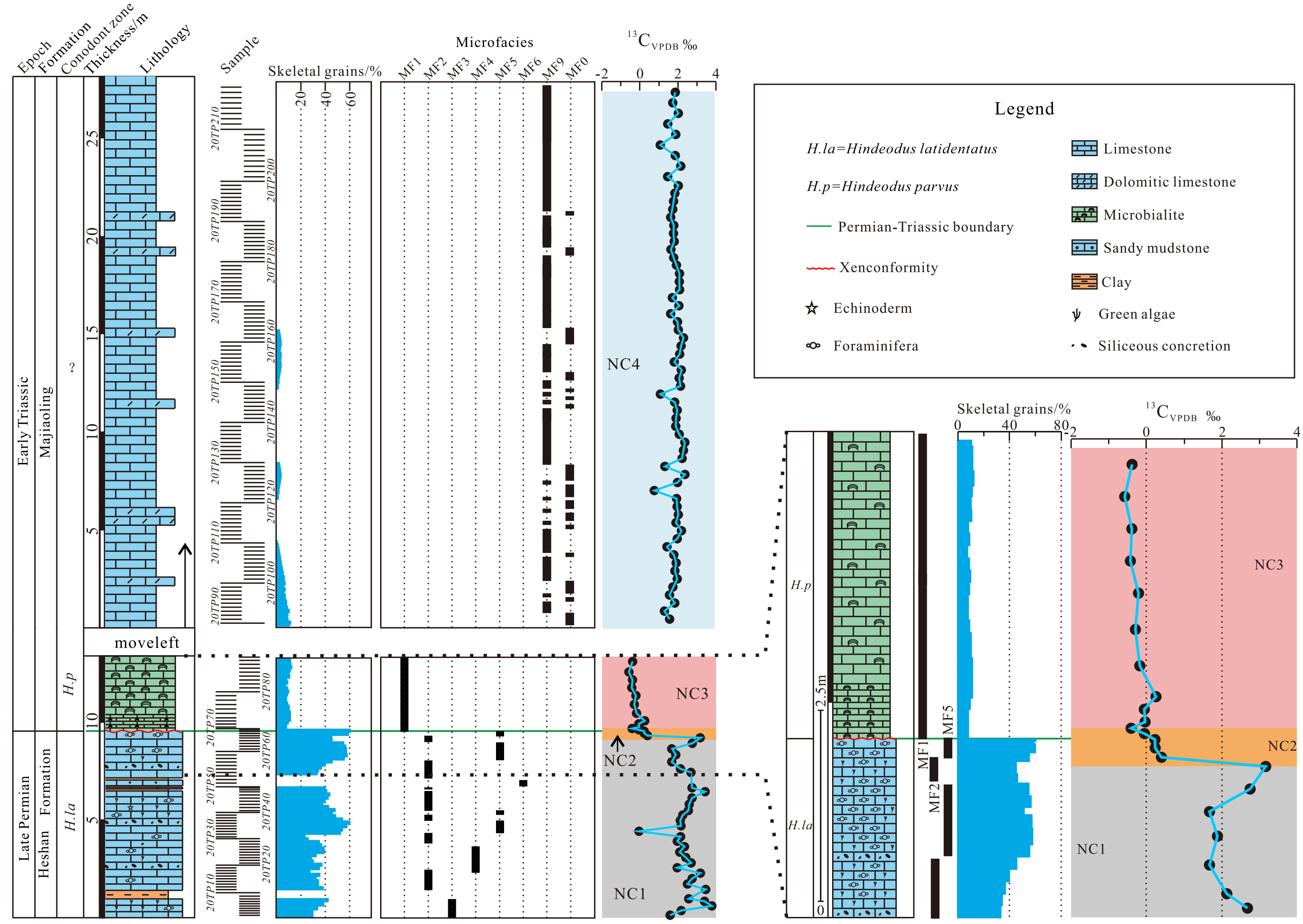

**Fig. 5.** Stratigraphic log of the Taiping section showing sampling locations, biostratigraphy, bioclast distribution, microfacies classification, whole-rock carbonate $\delta^{13}$C curve, enlarged view of NC2 stage and conodont zones after Lehrmann et al. (2003) and Xiao et al. (2018).

Bioturbation structures are predominantly observed in low-energy middle ramp to outer ramp environments (Flügel, 2010). As such, the micritic matrix, bioturbation structures and, biotic evidence indicate an outer ramp setting below storm wave base.

*4.1.3.2. MF14: calcisphere mudstone.* This microfacies is dominated by abundant calcispheres (3–10%) with microbioclasts (Fig. 3o). The matrix is mainly micrite. The micritic matrix and calcispheres indicate a low-energy outer-ramp environment (Flügel, 2010). MF14 is widely developed in the Garencuo Formation in the Wenbudangsang section (Fig. 6).

### 4.2. Carbon and oxygen isotopes

The $\delta^{13}C_{carb}$ profiles of the Liangfengya, Taiping, and Wenbudansang sections are similar, with significant NCIEs demarcating the PTB hyperthermal event in each section. Nevertheless, the magnitudes and stratigraphic thicknesses of the NCIE in each section differ (Figs. 4–6). For this study, the carbon-isotope evolution during the PTB hyperthermal event is divided into four stages: NC1 (before the onset of the CIE, pre-NCIE), NC2 (where $\delta^{13}C_{carb}$ values decline, NCIE onset), NC3 (sustained low $\delta^{13}C_{carb}$ values, NCIE body), and NC4 (the recovery stage of the NCIE, post-NCIE).

#### 4.2.1. Liangfengya section

In the Liangfengya section, $\delta^{13}C_{carb}$ values range from −3.8‰ to 3.3‰ with an average of −0.2‰, while $\delta^{18}O_{carb}$ values range from −11.2‰ to −5.3‰ with an average of −7.4‰ (Fig. 4). The $\delta^{13}C_{carb}$ average value of the NC1 stage is 2.7‰, which corresponds to the lower member of the Upper Permian Changxing Formation. The $\delta^{13}C_{carb}$ values of the NC2 stage gradually decrease from 2.2‰ to the lowest value of −1.3‰, except for one datapoint of −3.2‰ at 9.45 m, with a negative excursion magnitude of 3.5‰, which spans a stratigraphic thickness of 2.25 m. A xenoconformity (see Section 5.2.1) occurs at 0.45 m above the NC2 stage, and the PTB, defined by the FAD of *Hindeodus parvus*, is 1.45 m above the xenoconformity. The $\delta^{13}C_{carb}$ values of the NC3 stage are relatively constant (average of −1.3‰), and the NC3 stage belongs to the Early Triassic Feixianguan Formation.

#### 4.2.2. Taiping section

In the Taiping section, $\delta^{13}C_{carb}$ values range from −0.6‰ to 3.7‰ with an average of 1.7‰, whereas $\delta^{18}O_{carb}$ values range from −11.0‰ to −4.8‰ with an average of −6.1‰ (Fig. 5). The absence of the *Hindeodus praeparvus* conodont Zone implies a stratigraphic gap in this section, which is supported by a sharp NCIE. This inference is further supported by the comprehensive carbon-isotope curve of the Liangfengya and Wenbudangsang sections, which reveals that the missing conodont zone of the Taiping section corresponds to the NC2 stage (Figs. 1b and 5). This suggests that the FAD of *Hindeodus parvus* likely aligns with the xenoconformity observed at 0.40 m in the NC2 stage. The $\delta^{13}C_{carb}$ average value of the NC1 stage is 2.4‰, which corresponds to the lower member of the Late Permian Heshan Formation. The $\delta^{13}C_{carb}$ values in the NC2 stage exhibit a marked negative shift from 3.1‰ to −0.4‰ and a thickness of 0.65 m. This stage is also within the Heshan Formation. The

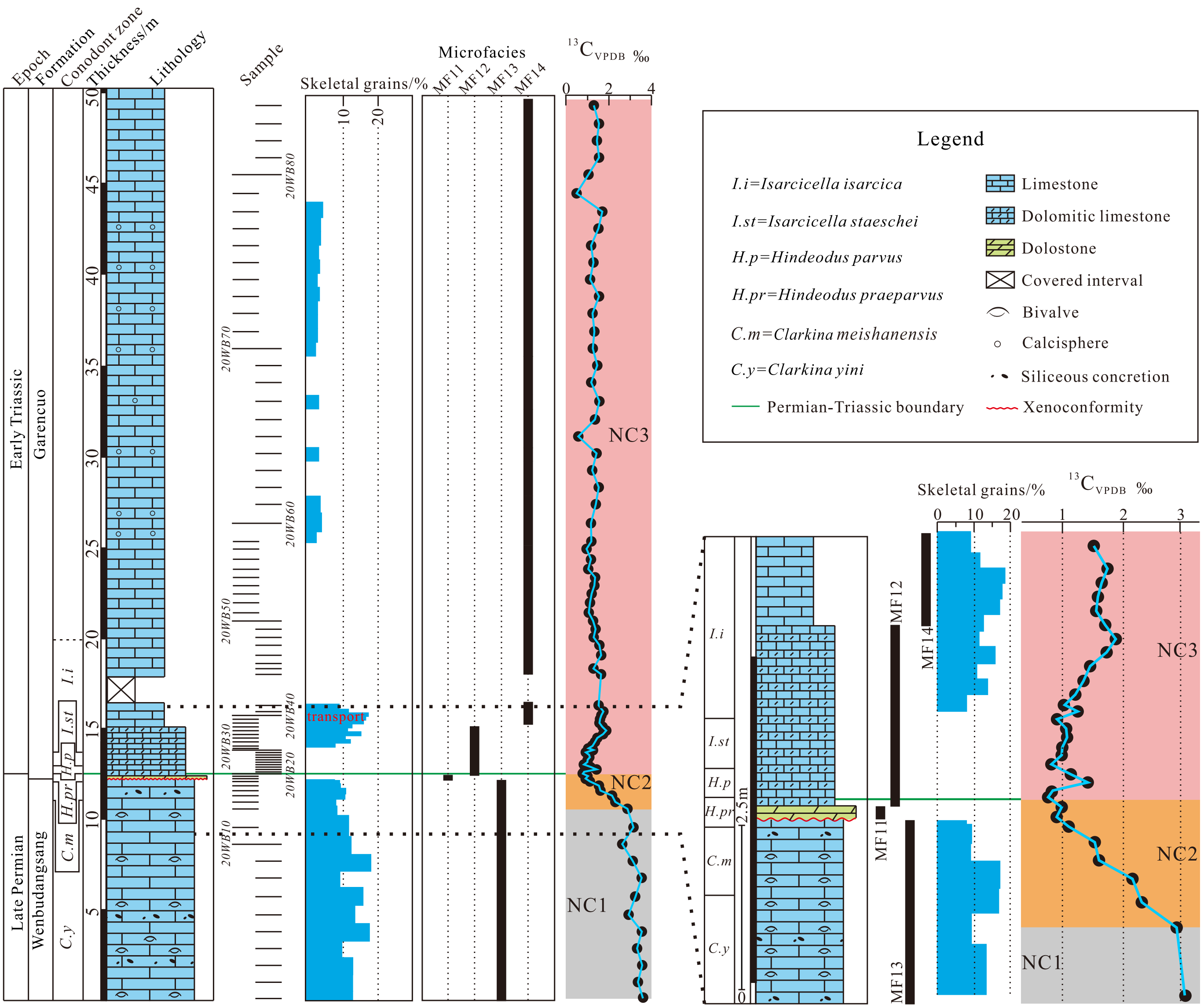

**Fig. 6.** Stratigraphic log of the Wenbudangsang section showing sampling locations, biostratigraphy, bioclast distribution, microfacies classification, whole-rock carbonate δ$^{13}$C curve, enlarged view of NC2 stage and conodont zones after Wu et al. (2014).

average δ$^{13}$C$_{carb}$ value of the NC3 stage is −0.2‰, corresponding to microbialite (MF1) of the Early Triassic Majiaoling Formation. Furthermore, the average δ$^{13}$C$_{carb}$ value of the NC4 stage is 1.8‰, which is similar to that of the NC1.

### 4.2.3. Wenbudangsang section

In the Wenbudangsang section, δ$^{13}$C$_{carb}$ values range from 0.5‰ to 3.6‰, with an average of 1.6‰, whereas δ$^{18}$O$_{carb}$ values range from −11.0 ‰ to −4.7‰, with an average of −6.1‰ (Fig. 6). The δ$^{13}$C$_{carb}$ average value of the NC1 stage is 3.2‰, which is high relative to the South China sections, and corresponds to the lower member of the Late Permian Wenbudangsang Formation. In the NC2 stage, the δ$^{13}$C$_{carb}$ values gradually decrease from 2.9‰ to 0.7‰, exhibiting a negative excursion of 2.2‰, and a thickness of 1.96 m. This encompasses some strata in the upper member of the Wenbudangsang Formation and the lower member of the Garenco Formation. A xenoconformity occurs 1.70 m above the negative excursion of the NC2 stage, and the PTB is 0.26 m above the xenoconformity. In the NC3 stage, the carbon isotopes maintain broadly consistent and low values (average = 1.3‰). This stage is within the Early Triassic Garenco Formation.

## 4.3. Evolution of depositional environments

The carbonate microfacies observed in the Liangfengya, Taiping, and Wenbudangsang sections provide insights into the sedimentary evolution of southern China and Lhasa during the latest Permian to earliest Triassic.

### 4.3.1. Liangfengya section

The NC1 stage in the Changxing Formation during the latest Permian is dominated by calcareous green algae wackestone (MF2) interbedded with benthic foraminiferal wackestone (MF3) deposited in a very shallow inner ramp environment (Fig. 4). The overlying NC2 stage in the lowermost part of Feixianguan Formation during the earliest Triassic is characterized by argillaceous bioclastic wackestone (MF7) and crinoidal wackestone (MF8), which represent a shallow inner ramp environment affected by terrigenous input. The NC3 stage in the lower part of the Feixianguan Formation is characterized by mudstone (MF9) interbedded with dolomitized mudstone (MF10), which suggests an inner ramp environment. The microfacies in the Liangfengya section record abrupt changes in biota and abundance during the NC2 stage.

#### 4.3.2. *Taiping section*

The NC1 stage in the Heshan Formation during the latest Permian is dominated by calcareous green algae wackestone (MF2) interbedded with benthic foraminiferal wackestone (MF3), calcareous spicule wackestone (MF4), bioclastic grainstone (MF5), and sandy mudstone (MF6). Together these indicate a very shallow inner ramp environment (Fig. 5). The NC2 stage was deposited in a very shallow inner ramp environment, similar to the NC1 stage, corresponding to the bioclastic grainstone (MF5) and microbialite (MF1). The NC3 stage in the lower part of the Majiaoling Formation is characterized by microbialite (MF1), which was replaced by mudstone (MF9) interbedded with dolomitized mudstone (MF10) during the NC4 stage in the middle to upper part of Majiaoling Formation. Like the microfacies in the Liangfengya section, those in the Taiping section also record abrupt changes in biota type and abundance during the NC2 stage.

#### 4.3.3. *Wenbudangsang section*

The NC1 and NC2 stage intervals within the Wenbudangsang Formation were characterized by burrowed bioclastic wackestone (MF13) deposited in an outer ramp environment (Fig. 6), which was abruptly replaced by fine-crystalline dolostone (MF11) at the base of the Garencuo Formation. The NC3 stage interval in the lower part of the Garencuo Formation is characterized by storm-affected mudstone (MF12) deposited in a middle ramp environment, which transitions to calcisphere mudstone (MF14) in the middle to the upper part of the Garencuo Formation, deposited in an outer ramp environment. In contrast to the Liangfengya and Taiping sections, this section records only a change in the abundance of biota during the NC2 stage, rather than a change in type as well. Although there are bioclasts in MF12, they were transported by storms rather than autochthonous.

## 5. Discussion

### 5.1. *Carbon-isotope stratigraphy comparison*

The isotopic signatures of carbon and oxygen in shallow marine carbonate rocks are prone to significant covariance due to meteoric diagenesis (Gross and Tracey, 1966; Knauth and Kennedy, 2009). As such, the correlation model of carbon and oxygen isotopes can be used to assess the degree of influence of meteoric diagenesis. Correlation analysis reveals no correlation between $\delta^{13}C_{carb}$ and $\delta^{18}O_{carb}$ in the Liangfengya, Taiping, and Wenbudangsang sections (Fig. 7; $R^2$ = 0.046, 0.099, and 0.075, respectively). In addition, a brief interval of terrigenous clast input (MF6) at 6.8 m in the Taiping section shows no corresponding change in $\delta^{13}C_{carb}$, suggesting negligible influence of terrestrial material on the carbon and oxygen isotope composition. Indeed, the carbon-isotope trends in the Liangfengya, Taiping, and Wenbudangsang sections correlate well with the trends observed at the global boundary stratotype section and point (GSSP) of the base Triassic at Meishan in South China (Cao et al., 2009; Burgess et al., 2014). In summary, the carbon and oxygen isotopes of the three sections underwent little to no alteration by diagenesis and thus likely reflect the composition of contemporaneous seawater.

All the sections show a marked shift (NC2) marking the onset of the PTB NCIE. In the Liangfengya, Taiping, and Wenbudangsan sections, the measured thickness of the NC2 stage is 2.25 m, 0.65 m, and 1.96 m, respectively (Fig. 8). The NC3 stage of the Early Triassic shows low carbon isotope values and small-scale fluctuations locally, just as observed in the deep-water sections of the Shangsi section in the Sichuan Basin (China) and at the Aras Valley section in Northwest Iran (Shen et al., 2013; Xie et al., 2017; Gliwa et al., 2020). However, only the Taiping section has a recovery stage (i.e., a stage characterized by a recovery in the $\delta^{13}C_{carb}$ signal back to pre-event values). It is not clear why the other sections do not record recovery stages.

### 5.2. *Sedimentary evolution during the PTB hyperthermal event*

High-precision U—Pb zircon dates from the Meishan section (GSSP) reveal that the duration of the NCIE is 660 kyr, with the NC2, NC3, and NC4 stages lasting 58 kyr, 432 kyr, and 170 kyr, respectively (Burgess et al., 2014) (Fig. 8). By using the duration of the NC2 stage from the Meishan section as a constant standard, the time scale of sedimentary events in our studied sections can be determined.

#### 5.2.1. *Xenoconformity and carbonate production crisis*

The presence of xenoconformities is evident in our studied sections, where they are recognized by abrupt changes in lithology and biological types or quantities (Figs. 4–6). During the NC2 stage, a large number of calcareous green algae and foraminifera developed in the Liangfengya section were replaced by echinoderms and bivalves, and the number of organisms also decreased sharply. The lithofacies also changed from MF3 (benthic foraminiferal wackestone) to MF7 (argillaceous bioclastic wackestone). In the Taiping section, the biological types also changed from foraminifera and calcareous green algae to microorganisms, and the lithofacies changed from MF5 (bioclastic grainstone) to MF1 (microbialite). Similarly, in the Wenbudangsang section, the sudden changes of lithofacies (from MF13: burrowed bioclastic wackestone to MF11: fine-crystalline dolostone) and the reduction or disappearance of organisms also occurred. At the same time, Calcareous green algae, fusulinids, rugose corals, trilobites, and radiolarians also completely disappeared during this stage worldwide. Leading to a prolonged reef gap and the disappearance of platform-margin reefs for >5 million years. (Song et al., 2012; Martindale et al., 2019; Li et al., 2023). Moreover, at the top of bed 27–2 of the Meishan section, there is also a feature consistent with a xenoconformity (Cao and Zheng, 2009; Zheng et al., 2013; Chen et al., 2015). Firstly, it represents a lithological and lithofacies transition surface with the overlying bed. Secondly, there are obvious differences in trace fossils and biological types above and below this interface. Finally, the abundance of biota decreases suddenly from 10 to 25% to 1–5% at this level. These changes are synchronous with the NC2 stage of the NCIE. Evidence from pyrite framboids and geochemistry confirm that extensive deoxygenation occurred in the Liangfengya, Taiping, and Wenbudangsang sections during the NC2 stage (Xiao et al., 2018; Ji et al., 2018; Li et al., 2021a). Such xenoconformities have been reported extensively during the PTB hyperthermal event from different sites. For example, in the Erlongkou section in Chongqing (China) and the Aras Valley section in Northwest Iran, the lithofacies abruptly changed from bioclastic limestone to claystone or mudstone across the NC2 stage (Gliwa et al., 2020; Li et al., 2021b). An abrupt change from bioclastic grainstone to microbialite occurs during the NC2 stage and also widespread in South China, as documented in Yin et al. (2014), Wang et al. (2019), and Zhang et al. (2020b). Thus, the presence of xenoconformities during the PTB hyperthermal event onset represents a clear sedimentological expression of the dramatic changes in the global paleoenvironment at this time.

Although xenoconformities are widely developed during the PTB hyperthermal event, the timing varies among different sections and corresponds to different stages of the NCIE. By using the duration of the NC2 stage (58 kyr; Burgess et al., 2014) as a benchmark, and assuming constant sedimentation rates for this relatively short interval, we determine that the xenoconformity in the inner ramp Liangfengya section occurred 12 kyr after the onset of the NCIE (i.e. 12 kyr after the start of NC1) (Fig. 9a). In the Taiping section, two scenarios are considered due to the lack of the *Hindeodus praeparvus* conodont zone (Lehrmann et al., 2003; Xiao et al., 2018). If the *Hindeodus praeparvus* Zone is missing due to incompleteness, then we could assume the NC2 stage has the same (or at least similar) thickness as the Liangfengya section because these sections were deposited in a similar inner ramp environment (as confirmed by microfacies analysis). If so, the xenoconformity in the Taiping section could be estimated to have occurred 11 kyr after the onset of the NCIE, which is similar to the timing in the Liangfengya

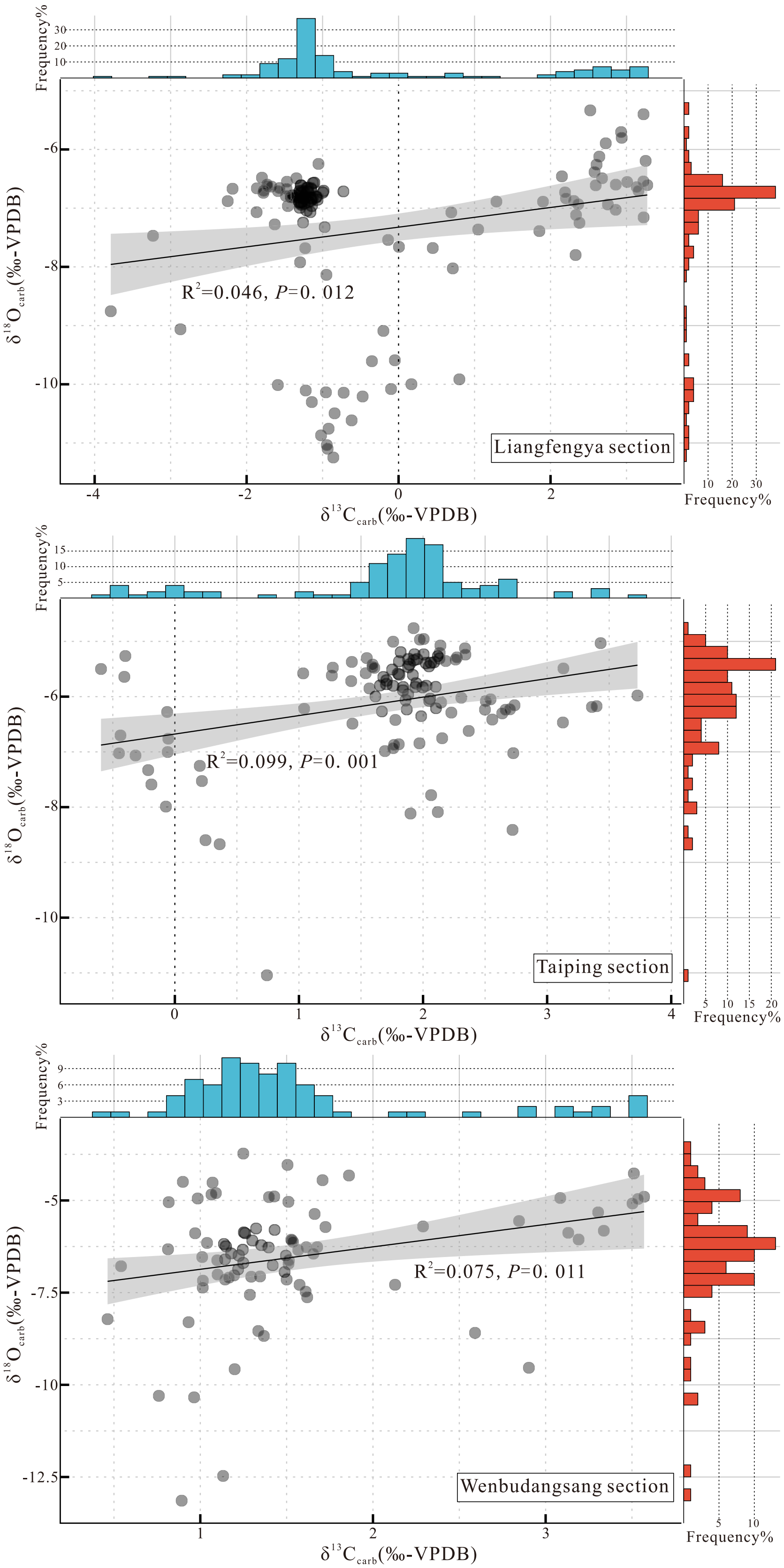

**Fig. 7.** Cross plot of bulk carbonate carbon isotopes versus oxygen isotopes for the Liangfengya, Taiping, and Wenbudangsang sections. Linear fit of $\delta^{13}C_{carb}$ and $\delta^{18}O_{carb}$ and the frequency of $\delta^{13}C_{carb}$ (blue bar graph) and $\delta^{18}O_{carb}$ (red bar graph) in the Liangfengya, Taiping, and Wenbudangsang sections, respectively. (For interpretation of the references to colour in this figure legend, the reader is referred to the web version of this article.)

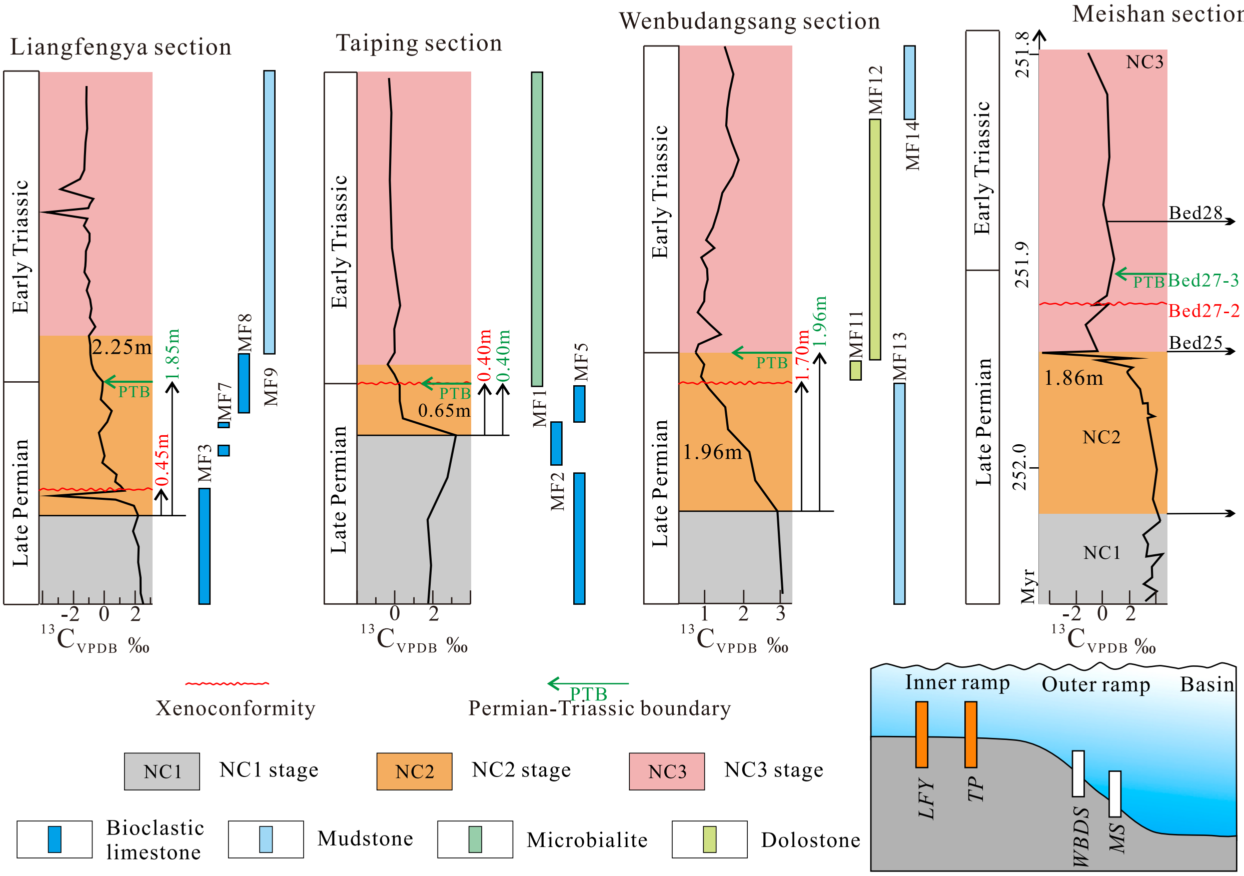

**Fig. 8.** Comparison of bulk carbonate carbon isotopes and microfacies in the Liangfengya, Taiping, Wenbudangsang, and Meishan sections. The thickness for each carbon isotope stage and the environment of each section is shown. The geochronology and carbon-isotope curve of the Meishan section are from Burgess et al. (2014) and Cao et al. (2009), respectively.

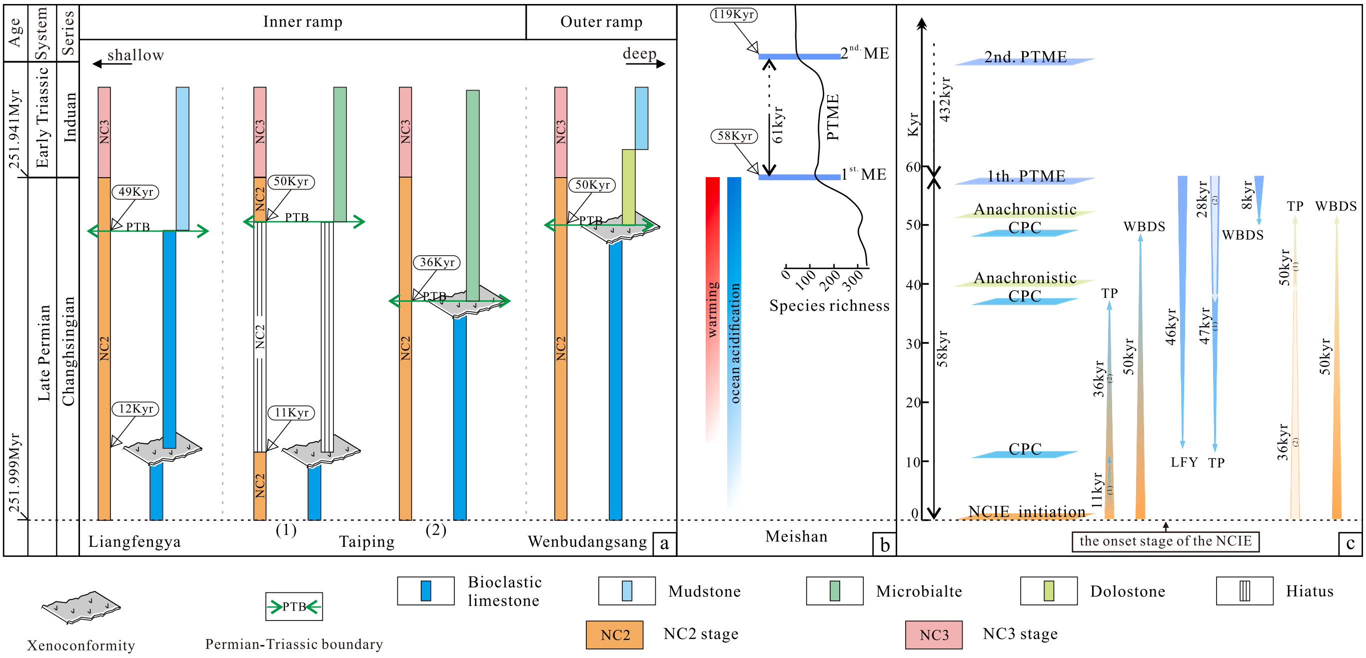

**Fig. 9.** Evolution of the hyperthermal event across the PTB. (a) Comparison of evolutionary succession of the Liangfengya, Taiping and Wenbudangsang sections showing xenoconformity development and timing of occurrence of anachronistic facies. (b) The species richness (Song et al., 2012) and environmental changes (Shen et al., 2019b) across the PTB mass extinction. (c) Geochronology and carbon-isotope curve of the Meishan section Burgess et al. (2014) and Cao et al. (2009), respectively. All dates (in kyr) are relative to NCIE onset (0 kyr). 1st. ME: the first extinction event; 2nd. ME: the second extinction; PTME: Permian–Triassic mass extinction; CPC: carbonate production crisis; NCIE: negative carbon isotope excursion; TP: Taiping section; WBDS: Wenbudangsang section; LFY: Liangfengya section.

section (Fig. 9a). Alternatively, if the *Hindeodus praeparvus* Zone was not found due to low sampling resolution, processing methods, or preservation conditions (cf. Shen et al., 2019a), and thus the stratigraphy is complete, then the xenoconformity in the Taiping section occurred ~36 kyr after the onset of NCIE (Fig. 9a). In contrast, the xenoconformity in the Wenbudangsang section is estimated to have occurred 50 kyr after the onset of the NCIE (Fig. 9a). Regardless of whether there is a stratigraphic gap in the Taiping section, the onset of the xenoconformity in the outer ramp Wenbudangsang section appears to be later than in the inner ramp Liangfengya and Taiping sections. In the Meishan section (outer ramp and deepest section, Fig. 8), the xenoconformity is located near the onset of the NC3 stage, 59 kyr after the NCIE onset (Fig. 8). Taken together, and despite uncertainties in the precise delineation and recognition of the NC2 stage, our observations show that xenoconformities developed earlier in shallower water settings compared to deeper water settings.

### 5.2.2. PTB and mass extinction

The PTB is defined based on the FAD of *Hindeodus parvus*. However, high-resolution biostratigraphy research shows that the FAD of *Hindeodus parvus* at the Zhongzhai section in Guizhou and the Daijiagou section in Chongqing occurs slightly earlier than in the Meishan GSSP section (Zhang et al., 2014; Yuan et al., 2015; Shen et al., 2019a). As mentioned above, this may be due to biological diachroneity, preservation conditions, and/or other reasons (cf. Shen et al., 2019a). During the NC2 stage, the Liangfengya and Taiping sections of the shallow-water inner ramp provide evidence for a distinct change in fossil species, where the autotrophic biological assemblages dominated by calcareous green algae and foraminifera gave way to heterotrophic biological assemblages, such as echinoderms, bivalves, or microorganisms (Figs. 4 and 5). The Wenbudangsang section of the outer ramp is primarily characterized by heterotrophic biotic assemblages and shows a sudden decrease in biotic abundance, rather than type, during the NC2 stage (Fig. 6). Subsequently, during the NC2 stage, these three studied sections underwent a transition to carbonates with low bioclast content and rarer bioturbation. Together, these changes reflect a marked and protracted deterioration of the carbonate platform environment and a crisis in carbonate production rate. The abrupt change in fossil assemblages and biotic content in the NC2 stage signifies the onset of this deterioration, reflected by xenoconformity development. In addition, the dominant biota in the NC2 stage shifted from metazoans to microorganisms, which may also indicate a decrease in carbonate production rate and provide evidence for a carbonate production crisis.

During the PTB hyperthermal event, two mass extinctions took place (Song et al., 2012). The first extinction event took place at bed 25 of the Meishan section, and the second extinction occurred at bed 28 of the Meishan section (Song et al., 2012). According to U—Pb zircon data, these two mass extinctions occurred 58 kyr and 119 kyr after the onset of the NCIE (Burgess et al., 2014). Thus, they are separated by a 61 kyr interval, with the first mass extinction at the NC2/NC3 stage boundary, and the second mass extinction within the NC3 stage (Fig. 9b). As mentioned above, the sudden change in biotic assemblages occurred 12 kyr after the onset of the NCIE in the Liangfengya section (Fig. 9a), and either 11 kyr or 36 kyr after the NCIE onset in the Taiping section (see discussion above) (Fig. 9a). These changes demonstrate that the timing of the carbonate production crisis preceded the mass extinction at Meishan by 46 kyr at Liangfengya, and by either 47 kyr or 28 kyr at Taiping (Fig. 9c). In the Wenbudangsang section, a notable reduction in fossil abundance occurred 50 kyr after the onset of the NCIE (Fig. 9a), which suggests that the deep-water outer ramp carbonate production crisis preceded the mass extinction by 8 kyr (Fig. 9c). The above-mentioned biotic changes suggest that regardless of the exact timing, the carbonate production crisis across the PTB was a gradual process expanding from shallow to deep water, which is consistent with the notion that redox changes propagate from shallow- to deep-water environments (Schobben et al., 2020).

### 5.2.3. Anachronistic facies and developmental timeframe

Anachronistic facies refer to a large number of unusual sedimentary facies and fabrics formed under the background of mass extinction and subsequent environmental stress, including microbialites, vermicular limestone, flat pebble conglomerates, and oolitic grainstones (Woods, 2014; Abdolmaleki and Tavakoli, 2016). The anachronistic facies can be compared to other contemporaneous deposits from around the world during the Late Permian and Early Triassic, especially during the PTB hyperthermal event (Woods, 2014). Microbialite is also a typical anachronistic deposit and is frequently observed across the PTB hyperthermal event elsewhere, such as at the Yangjiawan section in Hunan, the Zuodeng section in Guangxi, Xikou section in Shaanxi, and the Yudongzi and Xiejiacao sections in Sichuan (Deng et al., 2017; Zhang et al., 2020b; Chen et al., 2022a). The microbialites exhibit a variety of morphologies and textures, including dome-, dendroid-, clotted, or irregularly shaped structures when examined under a microscope (Riding, 2000; Wu et al., 2018). The microbialites in the Taiping section exhibit distinctive dendroid-shaped structures and are separated from the underlying bioclastic grainstone by the xenoconformity. The microbialites first occur in the NC2 stage at Taiping either 36 kyr or 50 kyr after the onset of the NCIE (see discussion above), and continued into the NC3 stage (Fig. 9a). In addition, Woods (2014) pointed out that microbial activity is an important factor in the formation of anachronistic facies. At the same time, Li et al. (2023) reported the ubiquitous presence of microbes in the dolomitic limestone or dolostone, which suggests the dolomite is another type of anachronistic facies. This is likely the same case for the dolomite (MF11) observed in the Wenbudangsang section, although no microbes were identified. Dolomite deposition started in the NC2 stage in the Wenbudangsang section, with the onset of this facies occurring 50 kyr after the onset of the NCIE (Fig. 9a).

## 5.3. Timing and driving factors of sedimentary changes across the PTB hyperthermal event

The above analyses indicate marked differences in the timing of sedimentological and biotic changes. Broadly, the following chronostratigraphic sequence of sedimentary events during the PTB hyperthermal event can be recognized: 1) onset of the NCIE, 2) carbonate production crisis (firstly affecting shallow water, then deeper water), 3) development of anachronistic deposits, 4) first and then second mass extinction (Fig. 9c).

Two mechanisms may be responsible for the carbonate production crisis. One potential explanation is fluctuations in sea level. As global sea-level rose, the paleo-water depth in mid and low latitudes deepened, creating favorable conditions for the formation of heterotrophic assemblages in a carbonate depositional environment below the euphotic zone (Carannante et al., 1988; Westphal et al., 2010). This is supported by microbialite-like carbonate dominated by fine-sized dolomites and calcites with abundant heterotrophic microbes appearing in deep-water areas during the PTB (Li et al., 2023), which generally have a lower production rate of carbonate than metazoans. During the carbonate production crisis, although microfacies analysis and xenoconformity development indicate sedimentary environment changes in the Liangfengya, Taiping, and Wenbudangsang sections, there is no clear evidence for paleo-water depth changes. This is also the case in the Julfa (Northwest Iran) and Baghuk Mountains (Central Iran) sections (Leda et al., 2014), indicating that fluctuations in paleo-water depth were not the main reason for the observed differences in the productivity crisis of the carbonate. Alternatively, the carbonate production crisis may have been related to abrupt climatic changes associated with the STLIP. Volcanic activity released a large amount of $CO_2$ and $SO_2$, which could have led to marked seawater acidification (Benjamin et al., 2014). On the other hand, enhanced continental weathering during the early phases of STLIP eruption (as suggested by Li isotopes, Cao et al., 2022) and consequent input of nutrients such as P and Fe, would lead to eutrophication and eukaryotic algae blooms (Shen et al., 2022b). Under these conditions, accompanied by enhanced primary productivity, seawater deoxygenation intensified (Schobben et al., 2020; Shen et al., 2022b). With the continued deterioration of the environment, the abundance and diversity of terrestrial plants, as well as soil stability, would have declined (Schobben et al., 2020; Dal Corso et al., 2022). Thus, enhanced hydrological cycling could have exacerbated soil erosion and physical weathering (Schobben et al., 2020), leading to further nutrient input and the exacerbation of hypoxic conditions. Under the dual environmental pressures of acidification and deoxygenation, marine biota could have migrated to safer deeper waters and/or higher latitudes (Song et al., 2018; Liu et al., 2020), leading to the carbonate production crisis in shallow water environment. The likely lower environmental pressure on deeper water (i.e., outer ramp settings), dominated by heterotrophic biotic assemblages, could be the reason that the carbonate production crisis began later in the Wenbudangsang section compared to the shallower inner ramp environments of the Liangfengya and Taiping sections.

## 6. Conclusions

In this study, three Permian–Triassic carbonate platform sections (Liangfengya, Taiping, and Wenbudangsang sections) were investigated to reconstruct their sedimentary evolution across the PTB hyperthermal event on millennial timescales. Our main findings are as follows:

(1) Carbonate microfacies analysis shows the Liangfengya and Taiping sections represent an inner ramp environment, whereas the Wenbudangsang section represents an outer ramp environment. Anachronistic facies (microbialite, and most probably dolomite) were identified, along with the presence of xenoconformities.
(2) Comparison of carbon-isotope data between the three studied sections shows that the changes in carbon isotopes across the PTB hyperthermal event can be divided into four stages: NC1 (before the onset of the NCIE), NC2 (the interval of decreasing $\delta^{13}C_{carb}$, i.e., the onset stage of the NCIE), NC3 (the interval of sustained low $\delta^{13}C_{carb}$, corresponding to the body of the NCIE), and NC4 (the recovery stage of the NCIE).
(3) An abrupt change in carbonate platform productivity is indicated by the appearance of xenoconformities. A xenoconformity formed in the shallow-water inner ramp environment 11 kyr after the NCIE and in the deep-water outer ramp environment 50 kyr after the NCIE.
(4) The sequence of depositional events across the PTB hyperthermal event was as follows: 1) the onset of the NCIE (presumably marking the onset of $^{12}C$-enriched carbon release from volcanism), 2) the carbonate production crisis (first in shallow water, later in deeper water), 3) the appearance of the anachronistic facies (microbialite and dolomite), 4) mass extinction.

Environmental stresses (likely acidification and anoxic environment) associated with STLIP volcanic activity were the probable triggers for the carbonate production crisis that our sections record.

## CRediT authorship contribution statement

**Jiawei He:** Writing – review & editing, Writing – original draft, Methodology, Investigation, Conceptualization. **Xiumian Hu:** Writing – review & editing, Methodology. **Juan Li:** Writing – review & editing, Supervision. **David B. Kemp:** Writing – review & editing, Validation. **Mingcai Hou:** Writing – review & editing. **Zhong Han:** Writing – review & editing, Supervision, Methodology, Funding acquisition, Formal analysis.

## Declaration of competing interest

The authors declare that they have no known competing financial interests or personal relationships that could have appeared to influence the work reported in this paper.

## Data availability

Data will be made available on request.

## Acknowledgments

We thank the constructive comments from Jingxin Jiang and Yiwei Xu, which greatly improved the quality of our manuscript. We also thank the four anonymous reviewers for their insightful comments and the editor for their enthusiastic assistance. This work was funded by the National Natural Science Foundation of China (Grant Nos. 42002121, 41888101, 91755209, 42072124). This is a contribution to the IGCP 739.

## References

Abdolmaleki, J., Tavakoli, V., 2016. Anachronistic facies in the early Triassic successions of the Persian Gulf and its palaeoenvironmental reconstruction. Paleogeogr. Paleoclimatol. Paleoecol. 446, 213–224. https://doi.org/10.1016/j.palaeo.2016.01.031.

Algeo, T.J., Henderson, C.M., Tong, J.N., Feng, Q.L., Yin, H.F., Tyson, R.V., 2013. Plankton and productivity during the Permian–Triassic boundary crisis: An analysis of organic carbon fluxes. Glob. Planet. Chang. 105, 52–67. https://doi.org/10.1016/j.gloplacha.2012.02.008.

Bagherpour, B., Bucher, H., Baud, A., Brosse, M., Vennemann, T., Martini, R., Guodun, K., 2017. Onset, development, and cessation of basal early Triassic microbialites (BETM) in the Nanpanjiang pull–apart Basin, South China Block. Gondwana Res. 44, 178–204. https://doi.org/10.1016/j.gr.2016.11.013.

Banner, F.T., Simmons, M.D., 1994. Calcareous algae and Foraminifera as Water–Depth Indicators: An Example from the Early Cretaceous Carbonates of Northeast Arabia. (Ed. I. P. Simmons, M.D.), Micropalaeontology and Hydrocarbon Exploration in the Middle East: British Micropalaeontological Society Publications Series, pp. 243–252.

Benjamin, A.B., Jean, F.L., Christine, A.S., Linda, T.E., Jeffrey, T.K., 2014. Acid rain and ozone depletion from pulsed Siberian Traps magmatism. Geology 42 (1), 67–70. https://doi.org/10.1130/G34875.1.

Burgess, S.D., Bowring, S., Shen, S.Z., 2014. High–precision timeline for Earth's most severe extinction. Proc. Natl. Acad. Sci. USA 111 (9), 3316–3321. https://doi.org/10.1073/pnas.1317692111.

Cao, C.Q., Zheng, Q.F., 2009. Geological event sequences of the Permian-Triassic transition recorded in the microfacies in Meishan section. Sci. China Ser. D-Earth Sci. 52 (10), 1529–1536. https://doi.org/10.1007/s11430-009-0113-0.

Cao, C.Q., Love, G.D., Hays, L.E., Wang, W., Shen, S.Z., Summons, R.E., 2009. Biogeochemical evidence for euxinic oceans and ecological disturbance presaging the end–Permian mass extinction event. Earth Planet. Sci. Lett. 281, 188–201. https://doi.org/10.1016/j.epsl.2009.02.012.

Cao, Y., Song, H.J., Algeo, T.J., Chu, D.L., Du, Y., Tian, L., Wang, Y.H., Tong, J., 2019. Intensified chemical weathering during the Permian–Triassic transition recorded in terrestrial and marine successions. Paleogeogr. Paleoclimatol. Paleoecol. 519, 166–177. https://doi.org/10.1016/j.palaeo.2018.06.012.

Cao, C., Bataille, C.P., Song, H.J., Saltzman, M.R., Cramer, K.T., Wu, H.C., Korte, C., Zhang, Z.F., Liu, X.M., 2022. Persistent late Permian to early Triassic warmth linked to enhanced reverse weathering. Nat. Geosci. 15, 832–838. https://doi.org/10.1038/s41561-022-01009-x.

Carannante, G., Esteban, M., Milliman, J.D., Simone, L., 1988. Carbonate lithofacies as paleolatitude indicators: problems and limitations. Sediment. Geol. 60 (1–4), 333–346. https://doi.org/10.1016/0037-0738(88)90128-5.

Carroll, A.R., 2017. Xenoconformities and the stratigraphic record of paleoenvironmental change. Geology 45 (7), 639–642. https://doi.org/10.1130/G38952.1.

Chen, Z.Q., Yang, H., Luo, M., Benton, M.J., Kaiho, K., Zhao, L.S., Huang, Y.G., Zhang, K.X., Fang, Y.H., Jiang, H.S., Qiu, H., Li, Y., Tu, C.Y., Shi, L., Zhang, L., Feng, X.Q., Chen, L., 2015. Complete biotic and sedimentary records of the Permian-Triassic transition from Meishan section, South China: Ecologically assessing mass extinction and its aftermath. Earth Sci. Rev. 149, 67–107. https://doi.org/10.1016/j.earscirev.2014.10.005.

Chen, J., Shen, S.Z., Li, X.H., Xu, Y.G., Joachimski, M.M., Bowring, S.A., Yuan, D.X., Chen, B., Zhang, H., Wang, Y., Cao, C.Q., Zheng, Q.F., Mu, L., 2016. High–resolution SIMS oxygen isotope analysis on conodont apatite from South China and implications for the end–Permian mass extinction. Paleogeogr. Paleoclimatol. Paleoecol. 448, 26–38. https://doi.org/10.1016/j.palaeo.2015.11.025.

Chen, J., Shen, S.Z., Zhang, Y.C., Angiolini, L., Gorgij, M.N., Crippa, G., Wang, W., Zhang, H., Yuan, D.X., Li, X.H., Xu, Y.G., 2020. Abrupt warming in the latest Permian detected using high–resolution in situ oxygen isotopes of conodont apatite from

Abadeh, Central Iran. Paleogeogr. Paleoclimatol. Paleoecol. 560, 109973 https://doi.org/10.1016/j.palaeo.2020.109973.

Chen, Z.Q., Fang, Y.H., Wignall, P.B., Guo, Z., Wu, S.Q., Liu, Z.L., Wang, R.Q., Huang, Y. G., Feng, X.X., 2022a. Microbial Blooms Triggered Pyrite Framboid Enrichment and Oxygen Depletion in Carbonate Platforms immediately after the latest Permian Extinction. Geophys. Res. Lett. 49 https://doi.org/10.1029/2021GL096998 e2021GL096998.

Chen, Z.Q., Harper, D.A.T., Grasby, S., Zhang, L., 2022b. Catastrophic event sequences across the Permian-Triassic boundary in the ocean and on land. Glob. Planet. Chang. 215, 103890 https://doi.org/10.1016/j.gloplacha.2022.103890.

Dal Corso, J., Song, H.J., Callegaro, S., Chu, D.L., Sun, Y.D., Hilton, J., Grasby, S.E., Joachimski, M.M., Wignall, P.B., 2022. Environmental crises at the Permian–Triassic mass extinction. Nat. Rev. Earth Environ. 3, 197–214. https://doi.org/10.1038/s43017-021-00259-4.

Deng, B.Z., Wang, Y.B., Woods, A., Li, S., Li, G.S., Chen, W.H., 2017. Evidence for rapid precipitation of calcium carbonate in South China at the beginning of early Triassic. Paleogeogr. Paleoclimatol. Paleoecol. 474, 187–197. https://doi.org/10.1016/j.palaeo.2016.06.007.

Dolenec, T., Ogorelec, B., Dolenec, M., Lojen, S., 2004. Carbon isotope variability and sedimentology of the Upper Permian carbonate rocks and changes across the Permian–Triassic boundary in the Masore section (Western Slovenia). Facies 50, 287–299. https://doi.org/10.1007/s10347-004-0016-7.

Du, Y., Song, H.Y., Tong, J.N., Algeo, T.J., Li, Z., Song, H.J., Huang, J.D., 2020. Changes in productivity associated with algal–microbial shifts during the early Triassic recovery of marine ecosystems. Geol. Soc. Am. Bull. 133 (1–2), 362–378. https://doi.org/10.1130/b35510.1.

Dunham, R.J., 1962. Classification of carbonate rocks according to deposition texture. In: I. P. Ham, W.E (Ed.), Classification of Carbonate Rocks, vol. 1. American Association of Petroleum Geologists, pp. 108–121.

Embry, A.F., Klovan, J.E., 1971. A late Devonian reef tract on Northeastern Banks Island, N.W.T. Bull. Can. Petrol. Geol. 19 (4), 730–781. https://doi.org/10.35767/gscpgbull.19.4.730.

Fan, J.X., Shen, S.Z., Erwin, D.H., Sadler, P.M., MacLeod, N., Cheng, Q.M., Yang, J., Wang, X.D., Wang, Y., Zhang, H., Chen, X., Li, G.X., Zhang, Y.C., Shi, Y.K., Yuan, D. X., Chen, Q., Zhang, L.N., Li, C., Zhao, Y.Y., 2020. A high–resolution summary of Cambrian to early Triassic marine invertebrate biodiversity. Science 367 (6475), 272–277. https://doi.org/10.1126/science.aax4953.

Fang, Z.Y., He, X.Q., Zhang, G.J., Zhang, X.L., Shen, Y.A., Qin, L.P., 2021. Ocean redox changes from the latest Permian to early Triassic recorded bychromium isotopes. Earth Planet. Sci. Lett. 570, 117050 https://doi.org/10.1016/j.epsl.2021.117050.

Feng, Z., Wei, H.B., Guo, Y., He, X.Y., Sui, Q., Zhou, Y., Guo, X.D., Lv, Y., 2020. From rainforest to herbland: New insights into land plant responses to the end–Permian mass extinction. Earth Sci. Rev. 204, 103153 https://doi.org/10.1016/j.earscirev.2020.103153.

Fio, K., Spangenberg, J.E., Vlahović, I., Sremac, J., Velić, I., Mrinjek, E., 2010. Stable isotope and trace element stratigraphy across the Permian–Triassic transition: A redefinition of the boundary in the Velebit Mountain. Croatia. Chem. Geol. 278, 38–57. https://doi.org/10.1016/j.chemgeo.2010.09.001.

Flügel, E., 2010. Microfacies of Carbonate Rocks: Analysis, Interpretation and Application, 2 nd ed. Springer-Verlag, Berlin Heidelberg New York, pp. 1–924. https://doi.org/10.1007/978-3-642-03796-2.

Foster, G.L., Hull, P., Lunt, D.J., Zachos, J.C., 2018. Placing our current 'hyperthermal' in the context of rapid climate change in our geological past. Phil. Trans. R. Soc. A 376, 20170086. https://doi.org/10.1098/rsta.2017.0086.

Gao, Y., Alan, R.C., Wang, C.S., 2021. Xenocomformity: a stratigraphic surface representing fundamental and abrupt paleoenvironmental change. Acta Sedimentol. Sin. 39 (1), 46–57. https://doi.org/10.14027/j.issn.1000-0550.2020.128. (in Chinese with English abstract).

Georgiev, S., Stein, H.J., Hannah, J.L., Bingen, B., Weiss, H.M., Piasecki, S., 2011. Hot acidic late Permian seas stifle life in record time. Earth Planet. Sci. Lett. 310 (3–4), 389–400. https://doi.org/10.1016/j.epsl.2011.08.010.

Gliwa, J., Ghaderi, A., Leda, L., Schobben, M., Tomás, S., Foster, W.J., Forel, M.B., Ghanizadeh Tabrizi, N., Grasby, S.E., Struck, U., Ashouri, A.R., Korn, D., 2020. Aras Valley (northwest Iran): high–resolution stratigraphy of a continuous central Tethyan Permian–Triassic boundary section. Foss. Rec. 23 (33–69), 2020. https://doi.org/10.5194/fr-23-33-2020.

Gross, M.G., Tracey, J.I., 1966. Oxygen and Carbon Isotopic Composition of Limestones and Dolomites, Bikini and Eniwetok Atolls. Science 151 (3714), 1082–1084. https://doi.org/10.1126/science.151.3714.1082.

Haas, J., Demény, A., Hips, K., Vennemann, T.W., 2006. Carbon isotope excursions and microfacies changes in marine Permian–Triassic boundary sections in Hungary. Paleogeogr. Paleoclimatol. Paleoecol. 237, 160–181. https://doi.org/10.1016/j.palaeo.2005.11.017.

Hinojosa, J.L., Brown, S.T., Chen, J., DePaolo, D.J., Paytan, A., Shen, S.Z., Payne, J., 2012. Evidence for end–Permian Ocean acidification from calcium isotopes in biogenic apatite. Geology 40 (8), 743–746. https://doi.org/10.1130/G33048.1.

Hips, K., Haas, J., 2009. Facies and diagenetic evaluation of the Permian–Triassic boundary interval and basal Triassic carbonates: shallow and deep ramp sections, Hungary. Facies 55, 421–442. https://doi.org/10.1007/s10347-009-0182-8.

Hu, X.M., Li, J., Han, Z., Li, Y., 2020. Two types of hyperthermal events in the Mesozoic–Cenozoic: Environmental impacts, biotic effects, and driving mechanisms. Sci. China Earth Sci. 63, 1041–1058. https://doi.org/10.1007/s11430-019-9604-4.

James, N.P., Jones, B., 2015. Origin of Carbonate Sedimentary Rocks. John Wiley & Sons, pp. 1–464.

Ji, C.J., Wu, Z.H., Yi, H.S., Xia, G.Q., Zhao, Z., Wang, T., 2018. $^{13}$C–$^{18}$O Isotopic Anomalous Study of the Carbonate Rock at the Wenbudangsang PTB Section, Tibe. Acta Geol. Sin. 92 (10), 2018–2027 (in Chinese with English abstract).

Jia, E.H., Song, H.J., 2018. End–Permian mass extinction of calcareous algae and microproblematica from Liangfengya, South China. Geobios 51, 401–418. https://doi.org/10.1016/j.geobios.2018.08.007.

Joachimski, M.M., Lai, X.L., Shen, S.Z., Jiang, H.S., Luo, G.M., Chen, B., Chen, J., Sun, Y. D., 2012. Climate warming in the latest Permian and the Permian–Triassic mass extinction. Geology 40 (3), 195–198. https://doi.org/10.1130/g32707.1.

Joachimski, M.M., Alekseev, A.S., Grigoryan, A., Gatovsky, Y.A., 2019. Siberian Trap volcanism, global warming and the Permian–Triassic mass extinction: New insights from Armenian Permian–Triassic sections. Geol. Soc. Am. Bull. 132 (1–2), 427–443. https://doi.org/10.1130/b35108.1.

Jurikova, H., Gutjahr, M., Wallmann, K., Flögel, S., Liebetrau, V., Posenato, R., Angiolini, L., Garbelli, C., Brand, U., Wiedenbeck, M., Eisenhauer, A., 2020. Permian–Triassic mass extinction pulses driven by major marine carbon cycle perturbations. Nat. Geosci. 13, 745–750. https://doi.org/10.1038/s41561-020-00646-4.

Kaiho, K., Aftabuzzaman, M., Jones, D.S., Tian, L., 2021. Pulsed volcanic combustion events coincident with the end-Permian terrestrial disturbance and the following global crisis. Geology 49 (3), 289–293. https://doi.org/10.1130/G48022.1.

Knauth, L.P., Kennedy, M.J., 2009. The late Precambrian greening of the Earth. Nature 460, 728–732. https://doi.org/10.1038/nature08213.

Korte, C., Kozur, H.W., 2010. Carbon–isotope stratigraphy across the Permian–Triassic boundary: A review. J. Asian Earth Sci. 39 (4), 215–235. https://doi.org/10.1016/j.jseaes.2010.01.005.

Leda, L., Korn, D., Ghaderi, A., Hairapetian, V., Struck, U., Reimold, W.U., 2014. Lithostratigraphy and carbonate microfacies across the Permian–Triassic boundary near Julfa (NW Iran) and in the Baghuk Mountains (Central Iran). Facies 60 (1), 295–325. https://doi.org/10.1007/s10347-013-0366-0.

Lehrmann, D.J., Payne, J.L., Felix, S.V., Dillett, P.M., Wang, H.M., Yu, Y.Y., Wei, J.R., 2003. Permian–Triassic Boundary Sections from Shallow–Marine Carbonate Platforms of the Nanpanjiang Basin, South China: Implications for Oceanic Conditions Associated with the End–Permian Extinction and Its Aftermath. Palaios 18 (2), 138–152. https://doi.org/10.1669/0883-1351(2003)18<138:pbsfsc>2.0.co;2.

Li, M.T., Song, H.J., Algeo, T.J., Wignall, P.B., Dai, X., Woods, A.D., 2018. A dolomitization event at the oceanic chemocline during the Permian–Triassic transition. Geology 46 (12), 1043–1046. https://doi.org/10.1130/g45479.1.

Li, M.T., Song, H.J., Woods, A.D., Dai, X., Wignall, P.B., 2019. Facies and evolution of the carbonate factory during the Permian–Triassic crisis in South Tibet, China. Sedimentology 66, 3008–3028. https://doi.org/10.1111/sed.12619.

Li, G.S., Liao, W., Li, S., Wang, Y.B., Lai, Z.P., 2021a. Different triggers for the two pulses of mass extinction across the Permian and Triassic boundary. Sci. Rep. 11, 6686. https://doi.org/10.1038/s41598-021-86111-7.

Li, J.Y., Liang, T., Zhu, X.E., Guo, Y.X., 2021b. Palaeoenvironmental implications of clay mineral characteristics in the Permian–Triassic transitional succession in the Erlongkou section, Fuling, Chongqing. Acta Geol. Sin. 95 (3), 868–882. https://doi.org/10.19762/j.cnki.dizhixuebao.2021110 (in Chinese with English abstract).

Li, M.T., Tian, L., Wignall, P.B., Dai, X., Lin, W., Cai, Q.S., Song, H.J., 2023. Expansion of microbial-induced carbonate factory into deeper water after the Permian-Triassic mass extinction. Glob. Planet. Chang. 230, 104274 https://doi.org/10.1016/j.gloplacha.2023.104274.

Liao, Z.W., Hu, W.X., Cao, J., Wang, X.L., Fu, X.G., 2020. Oceanic anoxia through the late Permian Changhsingian Stage in the lower Yangtze region, South China: evidence from sulfur isotopes and trace elements. Chem. Geol. 532, 119371 https://doi.org/10.1016/j.chemgeo.2019.119371.

Liu, S.A., Wu, H.C., Shen, S.Z., Jiang, G.Q., Zhang, S.H., Lv, Y.W., Zhang, H., Li, S.G., 2017. Zinc isotope evidence for intensive magmatism immediately before the end–Permian mass extinction. Geologys 45 (4), 343–346. https://doi.org/10.1130/g38644.1.

Liu, X.K., Song, H.J., Bond, D.P.G., Tong, J.N., Benton, M.J., 2020. Migration controls extinction and survival patterns of foraminifers during the Permian–Triassic crisis in South China. Earth Sci. Rev. 2020, 103329 https://doi.org/10.1016/j.earscirev.2020.103329.

Luo, G.M., Wang, Y.B., Algeo, T.J., Kump, L.R., Bai, X., Yang, H., Le, Y., Xie, S.C., 2011. Enhanced nitrogen fixation in the immediate aftermath of the latest Permian marine mass extinction. Geology 39 (7), 647–650. https://doi.org/10.1130/G32024.1.

Maaleki-Moghadam, M., Rafiei, B., Richoz, S., Woods, A.D., Krystyn, L., 2019. Anachronistic facies and carbon isotopes during the end-Permian biocrisis: evidence from the mid-Tethys (Kisejin, Iran). Paleogeogr. Paleoclimatol. Paleoecol. 516, 364–383. https://doi.org/10.1016/j.palaeo.2018.12.007.

Martindale, R.C., Foster, W.J., Velledits, F., 2019. The survival, recovery, and diversification of metazoan reef ecosystems following the end-Permian mass extinction event. Palaeogeogr. Palaeoclimatol. Palaeoecol. 513, 100–115. https://doi.org/10.1016/j.palaeo.2017.08.014.

Mays, C., McLoughlin, S., Frank, T.D., Fielding, C.R., Slater, S.M., Vajda, V., 2021. Lethal microbial blooms delayed freshwater ecosystem recovery following the end–Permian extinction. Nat. Commun. 12, 5511. https://doi.org/10.1038/s41467-021-25711-3.

Newby, S.M., Owens, J.D., Schoepfer, S.D., Algeo, T.J., 2021. Transient Ocean oxygenation at end–Permian mass extinction onset shown by thallium isotopes. Nat. Geosci. 14 (9), 678–683. https://doi.org/10.1038/s41561-021-00802-4.

Pérez-López, A., Pérez-Valera, F., 2011. Tempestite facies models for the epicontinental Triassic carbonates of the Betic Cordillera (southern Spain). Sedimentology 59 (2), 646–678. https://doi.org/10.1111/j.1365-3091.2011.01270.x.

Riding, R., 2000. Microbial carbonates: the geological record of calcified bacterial-algal mats and biofilms. Sedimentology 47 (s1), 179–214. https://doi.org/10.1046/j.1365-3091.2000.00003.x.

Sawada, K., Kaiho, K., Okano, K., 2012. Kerogen morphology and geochemistry at the Permian–Triassic transition in the Meishan section, South China: Implication for paleoenvironmental variation. J. Asian Earth Sci. 54-55, 78–90. https://doi.org/10.1016/j.jseaes.2012.04.004.

Schobben, M., Joachimski, M.M., Korn, D., Leda, L., Korte, C., 2014. Palaeotethys seawater temperature rise and an intensified hydrological cycle following the end–Permian mass extinction. Gondwana Res. 26 (2), 675–683. https://doi.org/10.1016/j.gr.2013.07.019.

Schobben, M., Foster, W.J., Sleveland, A.R.N., Zuchuat, V., Svensen, H.H., Planke, S., Bond, D.P.G., Marcelis, F., Newton, J.R., Wignal, P.B., Poulton, S.W., 2020. A nutrient control on marine anoxia during the end–Permian mass extinction. Nat. Geosci. 13 (9), 640–646. https://doi.org/10.1038/s41561-020-0622-1.

Shen, S.Z., Crowley, J.L., Wang, Y., Bowring, S.A., Erwin, D.H., Sadler, P.M., Cao, C.Q., Rothman, D.H., Henderson, C.M., Ramezani, J., Zhang, H., Shen, Y.A., Wang, X.D., Wang, W., Mu, L., Tang, Y.G., Liu, X.L., Liu, L.J., Zeng, Y., Jiang, Y.F., Jin, Y.G., 2011a. Calibrating the End–Permian Mass Extinction. Science 334 (6061), 1367–1372. https://doi.org/10.1126/science.1213454.

Shen, Y.A., Farquhar, J., Zhang, H., Masterson, A., Zhang, T.G., Wing, B.A., 2011b. Multiple S–isotopic evidence for episodic shoaling of anoxic water during late Permian mass extinction. Nat. Commun. 2, 210. https://doi.org/10.1038/ncomms1217.

Shen, S.Z., Cao, C.Q., Zhang, H., Bowring, S.A., Henderson, C.M., Payne, J.L., Davydov, V., Chen, B., Yuang, D.X., Zhang, Y.C., Wang, W., Zheng, Q.F., 2013. High–resolution $\delta^{13}C_{carb}$ chemostratigraphy from latest Guadalupian through earliest Triassic in South China and Iran. Earth Planet. Sci. Lett. 375, 156–165. https://doi.org/10.1016/j.epsl.2013.05.020.

Shen, J., Schoepfer, S.D., Feng, Q.L., Zhou, L., Yu, J.X., Song, H.Y., Wei, H.Y., Algeo, T.J., 2015. Marine productivity changes during the end–Permian crisis and early Triassic recovery. Earth Sci. Rev. 149, 136–162. https://doi.org/10.1016/j.earscirev.2014.11.002.

Shen, J., Feng, Q.L., Algeo, T.J., Li, C., Planavsky, N.J., Zhou, L., Zhang, M.L., 2016. Two pulses of oceanic environmental disturbance during the Permian–Triassic boundary crisis. Earth Planet. Sci. Lett. 443, 139–152. https://doi.org/10.1016/j.epsl.2016.03.030.

Shen, S.Z., Zhang, H., Zhang, Y.C., Yuan, D.X., Chen, B., He, W.H., Mu, L., Lin, W., Wang, W.Q., Chen, J., Wu, Q., Cao, C.Q., Wang, Y., Wang, X.D., 2019a. Permian integrative stratigraphy and timescale of China. Sci. China Earth Sci. 62, 154–188. https://doi.org/10.1007/s11430-017-9228-4.

Shen, S.Z., Ramezani, J., Chen, J., Cao, C.Q., Erwin, D.H., Zhang, H., Xiang, L., Schoepfer, S.D., Henderson, C.M., Zheng, Q.F., Bowring, S.A., Wang, Y., Li, X.H., Wang, X.D., Yuan, D.X., Zhang, Y.C., Mu, L., Wang, J., Wu, Y.S., 2019b. A sudden end–Permian Mass extinction in South China. Geol. Soc. Am. Bull. 131 (1–2), 205–223. https://doi.org/10.1130/B31909.1.

Shen, J., Yin, R.S., Algeo, T.J., Svensen, H.H., Schoepfer, S.D., 2022a. Mercury evidence for combustion of organic–rich sediments during the end–Triassic crisis. Nat. Commun. 13, 1307. https://doi.org/10.1038/s41467-022-28891-8.

Shen, J.H., Zhang, Y.G., Yang, H., Xie, S.C., Pearson, A., 2022b. Early and late phases of the Permian–Triassic mass extinction marked by different atmospheric $CO_2$ regimes. Nat. Geosci. 15, 839–844. https://doi.org/10.1038/s41561-022-01034-w.

Shen, S.Z., Zhang, Y.C., Yuan, D.X., Xu, H.P., Ju, Q., Zhang, H., Zheng, Q.F., Luo, M., Hou, Z.S., 2023. Integrative Permian stratigraphy, biotas, paleogeographical and paleoclimatic evolutions of the Qinghai-Tibetan Plateau and its surrounding areas. Sci. China-Earth Sci. https://doi.org/10.1007/s11430-023-1126-3.

Song, H.J., Wignall, P.B., Tong, J.N., Yin, H.F., 2012. Two pulses of extinction during the Permian–Triassic crisis. Nat. Geosci. 6 (1), 52–56. https://doi.org/10.1038/ngeo1649.

Song, H.J., Wignall, P.B., Dunhill, A.M., 2018. Decoupled taxonomic and ecological recoveries from the Permo-Triassic extinction. Sci. Adv. 4 (10), eaat5091. https://doi.org/10.1126/sciadv.aat5091.

Song, H.J., Kemp, D.B., Tian, L., Chu, D.L., Song, H.Y., Dai, X., 2021a. Thresholds of temperature change for mass extinctions. Nat. Commun. 12, 4694. https://doi.org/10.1038/s41467-021-25019-2.

Song, H.J., Song, H.Y., Tong, J.N., Gordon, G.W., Wignall, P.B., Tian, L., Zheng, W., Algeo, Tian J., Ling, L., Bai, R.Y., Wu, K., Anbar, A.D., 2021b. Conodont calcium isotopic evidence for multiple shelf acidification events during the early Triassic. Chem. Geol. 562, 120038 https://doi.org/10.1016/j.chemgeo.2020.120038.

Sun, Y.D., Joachimski, M.M., Wignall, P.B., Yan, C.B., Chen, Y.L., Jiang, H.S., Wang, L.N., Lai, X.L., 2012. Lethally hot temperatures during the early Triassic greenhouse. Science 338, 366–370. https://doi.org/10.1126/science.1224126.

Sun, H., Xiao, Y.L., Gao, Y.J., Zhang, G.J., Casey, J.F., Shen, Y.A., 2018. Rapid enhancement of chemical weathering recorded by extremely light seawater lithium isotopes at the Permian–Triassic boundary. Proc. Natl. Acad. Sci. USA 115 (15), 3782–3787. https://doi.org/10.1073/pnas.1711862115.

Sun, Y.D., Zulla, M.J., Joachimski, M.M., Bond, D.P.G., Wignall, P.B., Zhang, Z.T., Zhang, M.H., 2019. Ammonium ocean following the end–Permian mass extinction. Earth Planet. Sci. Lett. 518, 211–222. https://doi.org/10.1016/j.epsl.2019.04.036.

Tang, H., Kershaw, S., Liu, H., Tan, X.C., Li, F., Hu, G., Huang, C., Wang, L.C., Lian, C.B., Li, L., Yang, X.F., 2017. Permian–Triassic boundary microbialites (PTBMs) in southwest China: implications for paleoenvironment reconstruction. Facies 63, 1–23. https://doi.org/10.1007/s10347-016-0482-8.

Tian, L., Tong, J.N., Sun, D.Y., Xiong, Y.L., Wang, C.G., Song, H.J., Song, H.Y., Huang, Y. F., 2014. The microfacies and sedimentary responses to the mass extinction during the Permian–Triassic transition at Yangou Section, Jiangxi Province, South China. Sci. China Earth Sci. 57 (9), 2195–2207. https://doi.org/10.1007/s11430-014-4869-5.

Tian, L., Tong, J.N., Xiao, Y.F., Benton, M.J., Song, H.Y., Song, H.J., Liang, L., Wu, K., Chu, D.L., Algeo, T.J., 2019. Environmental instability prior to end–Permian mass extinction reflected in biotic and facies changes on shallow carbonate platforms of the Nanpanjiang Basin (South China). Paleogeogr. Paleoclimatol. Paleoecol. 519, 23–36. https://doi.org/10.1016/j.palaeo.2018.05.011.

Wang, Y., Sadler, P.M., Shen, S.Z., Erwin, D.H., Zhang, Y.C., Wang, X.D., Wang, W., Crowley, J.L., Henderson, C.M., 2014. Quantifying the process and abruptness of the end–Permian mass extinction. Paleobiology 40 (1), 113–129. https://doi.org/10.1666/13022.

Wang, T., Burne, R.V., Yuan, A.H., Wang, Y.B., Yi, Z.X., 2019. The evolution of microbialite forms during the early Triassic transgression: a case study in Chongyang of Hubei Province, South China. Paleogeogr. Paleoclimatol. Paleoecol. 2019, 209–220. https://doi.org/10.1016/j.palaeo.2018.01.043.

Warthmann, R., Lith, Y., Vasconcelos, C., McKenzie, J.A., Karpoff, A.M., 2000. Bacterially induced dolomite precipitation in anoxic culture experiments. Geology 28 (12), 1091–1094. https://doi.org/10.1130/0091-7613(2000)28<1091:bidpia>2.0.co;2.

Westphal, H., Halfar, J., Freiwald, A., 2010. Heterozoan carbonates in subtropical to tropical settings in the present and past. Int. J. Earth Sci. 99, 153–169. https://doi.org/10.1007/s00531-010-0563-9.

Wignall, P.B., Twitchett, R.J., 1999. Unusual intraclastic limestones in lower Triassic carbonates and their bearing on the aftermath of the end-Permian mass extinction. Sedimentology 46, 303–316. https://doi.org/10.1046/j.1365-3091.1999.00214.x.

Woods, A.D., 2014. Assessing early Triassic paleoceanographic conditions via unusual sedimentary fabrics and features. Earth Sci. Rev. 137, 6–18. https://doi.org/10.1016/j.earscirev.2013.08.015.

Wu, G.C., Ji, Z.S., Julie, A., Trotter Yao, J.X., Zhou, L.Q., 2014. Conodont biostratigraphy of a new Permo–Triassic boundary section at Wenbudangsang, north Tibet. Palaeogeogr. Palaeoclimatol. Palaeoecol. 411, 188–207. https://doi.org/10.1016/j.palaeo.2014.06.016.

Wu, Y.S., Jiang, H.X., Yu, G.L., Liu, L.J., 2018. Conceptions of microbialites and origin of the Permian-Triassic boundary microbialites from Laolongdong, Chongqing, China. J. Palaegeogr. - Chinese. 20 (5), 737–775. https://doi.org/10.7605/gdlxb.2018.05.053. (in Chinese with English abstract).

Wu, G.C., Ji, Z.S., Jurkovšek, K.T., Yao, J.X., Lash, G.G., 2021. Early Triassic Pachycladina fauna newly found in the southern Lhasa Terrane of Tibet and its palaeogeographic implications. Paleogeogr. Paleoclimatol. Paleoecol. 562, 110030 https://doi.org/10.1016/j.palaeo.2020.110030.

Xiao, Y.F., Wu, K., Tian, L., Benton, M.J., Du, Y., Yang, H., Tong, J.N., 2018. Framboidal pyrite evidence for persistent low oxygen levels in shallow–marine facies of the Nanpanjiang Basin during the Permian–Triassic transition. Paleogeogr. Paleoclimatol. Paleoecol. 511, 243–255. https://doi.org/10.1016/j.palaeo.2018.08.012.

Xie, S.C., Algeo, T.J., Zhou, W.F., Ruan, X.Y., Luo, G.M., Huang, J.H., Yan, J.X., 2017. Contrasting microbial community changes during mass extinctions at the Middle–Late Permian and Permian–Triassic boundaries. Earth Planet. Sci. Lett. 460, 180–191. https://doi.org/10.1016/j.epsl.2016.12.015.

Xu, Z., Hilton, J., Yu, J.X., Wignall, P.B., Yin, H.F., Xue, Q., Ren, W.J., Li, H., Shen, J., Meng, F.S., 2022. End Permian to Middle Triassic plant species richness and abundance patterns in South China: Coevolution of plants and the environment through the Permian–Triassic transition. Earth Sci. Rev. 232, 104136 https://doi.org/10.1016/j.earscirev.2022.104136.

Xu, G.Z., Shen, J., Algeo, T.J., Yu, J.X., Feng, Q.L., Frank, T.D., Fielding, C.R., Yan, J.X., Deconink, J.F., Lei, Y., 2023. Limited change in silicate chemical weathering intensity during the Permian–Triassic transition indicates ineffective climate regulation by weathering feedbacks. Earth Planet. Sci. Lett. 616, 118235 https://doi.org/10.1016/j.epsl.2023.118235.

Yin, H.F., Jiang, H.S., Xia, W.C., Feng, Q.L., Zhang, N., Shen, J., 2014. The end–Permian regression in South China and its implication on mass extinction. Earth Sci. Rev. 137, 19–33. https://doi.org/10.1016/j.earscirev.2013.06.003.

Yu, J.X., Broutin, J., Chen, Z.Q., Shi, X., Li, H., Chu, D.L., Huang, Q.S., 2015. Vegetation changeover across the Permian–Triassic Boundary in Southwest China. Earth Sci. Rev. 149, 203–224. https://doi.org/10.1016/j.earscirev.2015.04.005.

Yuan, D.X., Shen, S.Z., 2011. Conodont succession across the Permian–Triassic boundary of the Liangfengya section, Chongqing, South China. Acta Palaeontol. Sin. 50 (4), 420–438 (in Chinese with English abstract).

Yuan, D.X., Chen, J., Zhang, Y.C., Zheng, Q.F., Shen, S.Z., 2015. Changhsingian conodont succession and the end-Permian mass extinction event at the Daijiagou section in Chongqing, Southwest China. J. Asian Earth Sci. 105, 234–251. https://doi.org/10.1016/j.jseaes.2015.04.002.

Zhang, Y., Shi, G.R., He, W.H., Zhang, K.X., Wu, H.T., 2014. A new Changhsingian (late Permian) brachiopod fauna from the Zhongzhai section (South China), part 2: Lingulida, Orthida, Orthotetida and Spiriferida. Alcheringa 38, 480–503. https://doi.org/10.1080/03115518.2014.906167.

Zhang, F.F., Shen, S.Z., Cui, Y., Lenton, T.M., Dahl, T.W., Zhang, H., Zheng, Q.F., Wang, W.Q., Krainer, K., Anbar, A.D., 2020a. Two distinct episodes of marine anoxia during the Permian–Triassic crisis evidenced by uranium isotopes in marine dolostones. Geochim. Cosmochim. Acta 287, 165–179. https://doi.org/10.1016/j.gca.2020.01.032.

Zhang, X.Y., Wang, W.Q., Yuan, D.X., Zhang, H., Zheng, Q.F., 2020b. Stromatolite-dominated microbialites at the Permian–Triassic boundary of the Xikou section on South Qinling Block, China. Palaeoworld 29, 126–136. https://doi.org/10.1016/j.palwor.2019.05.009.

Zhang, H., Zhang, F.F., Chen, J.B., Erwin, D.H., Syverson, D.D., Ni, P., Rampino, M., Chi, Z., Cai, Y.F., Xiang, L., Li, W.Q., Liu, S.A., Wang, R.C., Wang, X.D., Feng, Z., Li, H.M., Zhang, T., Cai, H.M., Zheng, W., Cui, Y., Zhu, X.K., Hou, Z.Q., Wu, F.Y., Xu, Y.G., Planavsky, N., Shen, S.Z., 2021. Felsic volcanism as a factor driving the end-Permian mass extinction. Sci. Adv. 7, eabh1390. https://doi.org/10.1126/sciadv.abh1390.

Zheng, Q.F., Cao, C.Q., Zhang, M.Y., 2013. Sedimentary features of the Permian-Triassic boundary sequence of the Meishan section in Changxing County, Zhejiang Province. Sci. China Earth Sci. 56, 956–969. https://doi.org/10.1007/s11430-013-4602-9.

Zhou, Y.A., Cheng, X., Yu, L., Yang, X.F., Su, H.L., Peng, X.M., Xue, Y.K., Li, Y.Y., Ye, Y.K., Zhang, J., Li, Y.Y., Wu, H.N., 2016. Paleomagnetic study on the Triassic rocks from the Lhasa Terrane, Tibet, and its paleogeographic implications. J. Asian Earth Sci. 121, 108–119. https://doi.org/10.1016/j.jseaes.2016.02.006.

Ziegler, A.M., Hulver, M.L., Rowley, D.B., 1997. Permian world topography and climate. In: Martini, I.P. (Ed.), Late Glacial and Postglacial Environmental Changes–Quaternary, Carboniferous–Permian and Proterozoic. Oxford University Press, New York, pp. 111–146.